Flight Dynamics and Maneuver Loads on a Commercial Aircraft with Discrete Source Damage

Jeffrey A. Ouellette

Thesis submitted to the Faculty of the
Virginia Polytechnic Institute and State University
in partial fulfillment of the requirements for the degree of

Masters of Science
in
Aerospace Engineering

Mayuresh J. Patil, Chair
Rakesh K. Kapania
Craig A. Woolsey

April 26, 2010
Blacksburg, Virginia

Keywords: Damaged Aircraft, Flight Dynamics, Maneuver Loads

Flight Dynamics and Manuever Loads on a Commercial Aircraft with Discrete Source Damage

Jeffrey Ouellette

(ABSTRACT)

To improve the recoverability and survivability of aircraft after damage, a better understanding of the flight dynamics and the structural loads is needed. However, damage can introduce asymmetries that complicate the modeling. An extended vortex lattice code is used to model the quasi-steady aerodynamic forces. The vortex lattice method provides the force distribution which is not available elsewhere. Snapshots from the vortex lattice model are used to generate a reduced order model (ROM). This ROM contains non-linear terms to account for non-linearities that the damage can introduce. The ROM is coupled with equations of motion which are able to account for instantaneous shifts in the center of gravity caused by the damage. This methodology is applied to the generic transport model (GTM) with the loss of a portion of the port wing tip. This model is used to examine the effects of the damage on the aircraft's trim and the stability of that trim. This model is also used to calculate the aerodynamic, inertial, and propulsive loads on the wing as the aircraft is maneuvering.

Contents

List of Figures

List of Tables

Nomenclature

$\bar{q}$	Dynamic pressure
Δx, Δy, Δz	Center of gravity location in the body axis
$\hat{p}$	Non-dimensional roll rate, $\frac{bp}{2V}$
$\hat{q}$	Non-dimensional pitch rate, $\frac{\bar{c}p}{2V}$
$\hat{r}$	Non-dimensional yaw rate, $\frac{br}{2V}$
ϕ, θ, ψ	Euler angles of Body Axis in Inertial Frame
I_{xx}, I_{yy}, I_{zz}	Aircraft moment of inertia about the body axis
I_{xy}, I_{xz}, I_{yz}	Aircraft product of inertia about the body axis
p, q, r	Body axis angular velocities
S	Undamaged wing planform area
u, v, w	Body axis linear velocities
M	Mach number
m	Aircraft mass
$\mathbf{\Delta}$	Center of gravity location vector

ω	Angular velocity vector
$\mathbf{F}$	Total external forces
$\mathbf{M}$	Total external moments
$\mathbf{v}$	Linear velocity vector
$\boldsymbol{\mathcal{C}}^{A/B}$	Directional cosine matrix to A from B
$\mathbb{I}_3$	3×3 identity matrix
$\mathbf{I}$	Aircraft inertia matrix
$\mathbf{C}$	Aerodynamic coefficient matrix
$\mathbf{K}$	Aerodynamic correction factor matrix
c	Wing chord
m'	Wing mass distribution
W_{TO}	Aircraft take-off weight (in pounds)
W_{wing}	Weight of the wing
ω_{dr}	Dutch-roll mode natural frequency
ω_p	Phugoid mode natural frequency
ω_{sp}	Short period mode natural frequency
τ_r	Roll mode time constant
τ_s	Spiral mode time constant
ζ_{dr}	Dutch-roll mode damping ratio
ζ_p	Phugoid mode damping ratio

ζ_{sp}	Short period mode damping ratio

SUBSCRIPTS

avl	AVL Output
dmg	Of the damaged aircraft
exp	Experimental Data

SUPERSCRIPTS

A/B	Origin of axis A with respect to axis B
B	Body axis system
I	Inertial axis system
L	Local structural axis system
S	Stability axis system

Chapter 1

Introduction

1.1 Motivation

Loss of control (LOC) is a leading cause of commercial aircraft accidents[2]. An accident is attributed to LOC when the aircraft exceeds its normal flight envelope, such as a very large angle of attack or excessive wing loading. These upsets can be caused by or exacerbated by the presence of damage to the aircraft. Damage can alter the aerodynamic and inertial properties of the aircraft leading to a change in the aircraft's performance. Structural damage may weaken the aircraft, further reducing the aircraft's flight envelope.

To reduce the occurrence of LOC events, the Commercial Aviation Safety Team (CAST) chartered the Loss of Control (LOC) Joint Safety Analysis Team (JSAT)[3] in the 1990's. The JSAT identified several procedural changes and changes in pilot training to reduce the rate of LOC incidents

In 1999 NASA began the Aviation Safety and Security Program, later renamed the Aviation Safety Program (AvSP), with the goal of increasing the safety of the future commercial fleet[4]. As part of the AvSP, the Integrated Resilient Aircraft Control (IRAC) Project[5] was established to create control methods to reduce the occurrence of and improve the recoverability from these LOC events. IRAC has primarily focused on developing adaptive control

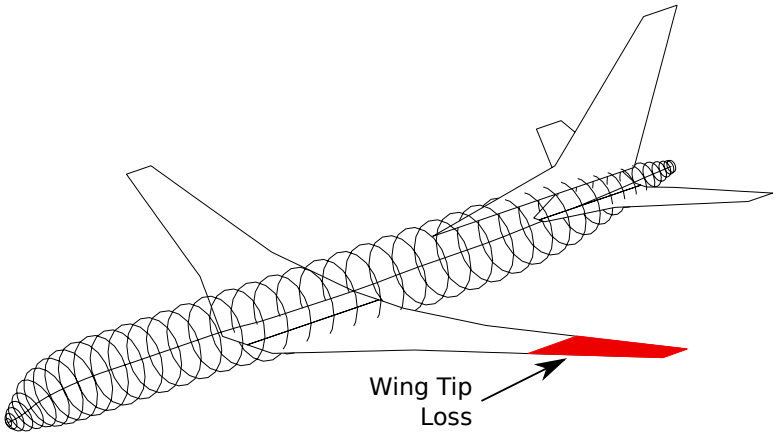

Figure 1.1: Illustration of Wing Tip Loss

laws and metrics for evaluation of these adaptive control laws. As part of the evaluation of these adaptive laws it is important to consider the effect on both the nominal and the damaged aircraft's structure. The first step to achieving this is a computationally efficient model of the aircraft's motion and the loads on the aircraft's structure.

1.2 Objectives

For the present work the Generic Transport Model (GTM), a 5.5% scale model of a modern commercial aircraft, is considered. This subscale aircraft has been developed for the testing of experimental control laws as part of the IRAC project. The damage considered is the loss of the port wing tip as shown in Fig. 1.1. The amount of the damage is the percentage of the half-span lost. This damage is assumed to occur instantly, and no impact forces are considered. The first objective is to be able to model the rigid body motion (flight dynamics) of the GTM due to the control inputs as the damage changes. This requires the forces acting on the complete aircraft shown in blue in Fig. 1.2. The loss of the wing tip leads to an asymmetric aircraft configuration, producing coupling between the longitudinal and lateral motion. To accurately capture the aerodynamic forces, including the effect of an asymmetric wake, a 3-D aerodynamic model is needed. Most existing methods are too slow for direct integration, so a reduced-order model (ROM) capable of modeling non-linearities due to the

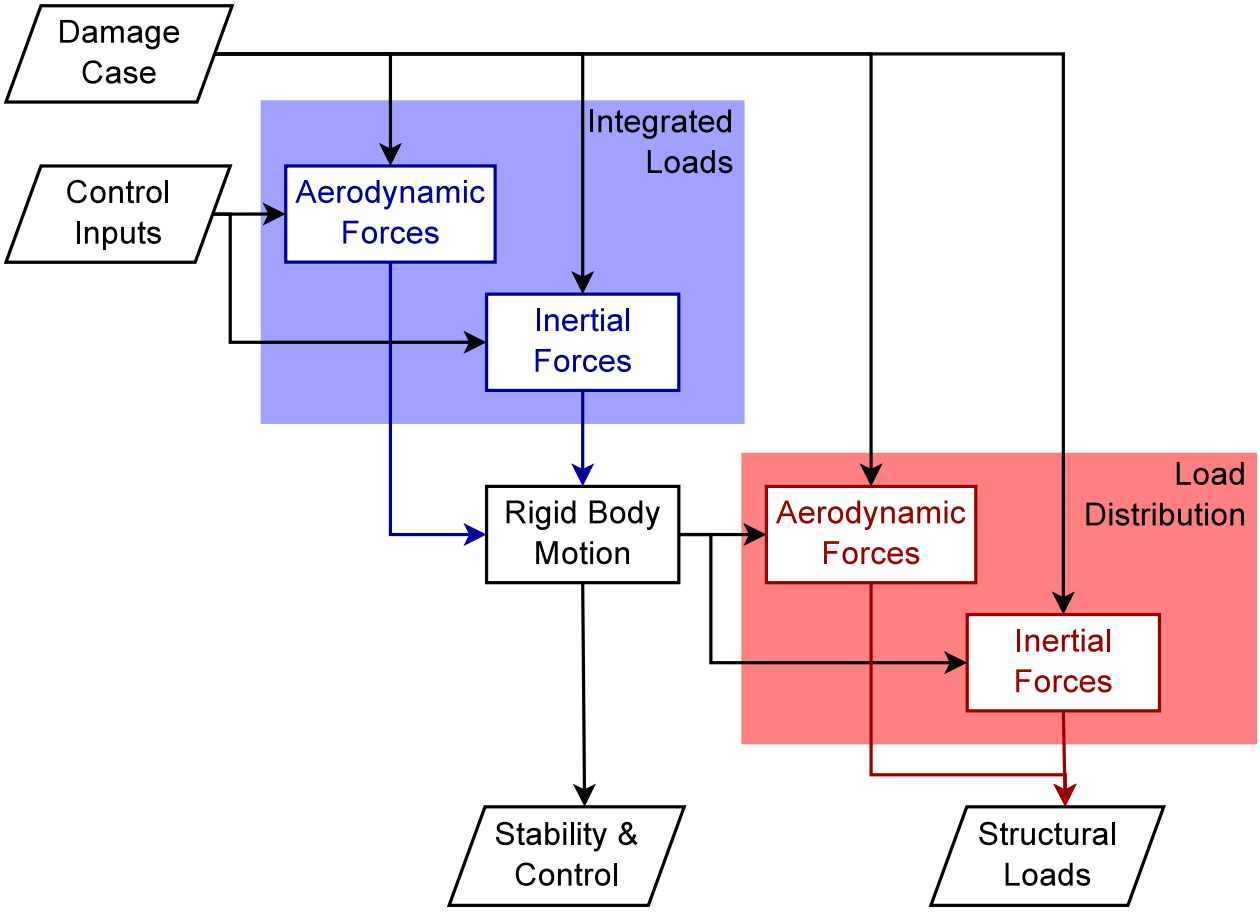

Figure 1.2: Methodology for Structural Loads of a Damaged Aircraft

drag and those introduced by the damage is needed. It is also important for this model to be able to handle the instantaneous shift in the aircraft's center of gravity which will occur when the wing tip is lost.

With a symmetric aircraft the aircraft's motion can be separated into longitudinal and lateral motion by locating the body axis at the aircraft's center of gravity. The asymmetries of the damage and the instantaneous shifts in the center of gravity preclude this simplification. The damage also complicates the calculation of a trim condition for the non-linear equations of motion since the control surfaces must cancel the side force, rolling moment, and yawing moment which the damage may introduce. Linearization of the equations of motion about this trim will allow examination of the effect of this coupling on the traditional rigid body modes (phugoid, Dutch roll, short period, etc.), and the stability of this trim.

The final objective of the current research is to calculate the structural forces on the undamaged and damaged aircraft as a response to the rigid body motion. This objective is represented in red in Fig. 1.2. Again a ROM is needed which will account for 3-D effects and for the non-linearities. Additionally, the ROM must be able to account for complex variations in the distribution due to control surfaces.

Chapter 2

Literature Review

For investigating loss of control (LOC) events NASA Langley has developed subscale models of commercial aircraft known as AirSTAR. Details of the S-2 aircraft, the first of these subscale aircraft, and the associated ground facilities are discussed by Cunningham et al.[6]. The S-2 Aircraft is an off-the-shelf model fitted with additional instrumentation. This aircraft was used for initial development of the procedures and ground facilities. This allows testing and development without risking the more sophisticated and more expensive dynamically scaled aircraft. The AirSTAR facilities are able to determine real time estimates of the aircraft's aerodynamic parameters. This is needed since no windtunnel data is available for the S-2, and for validation of windtunnel data on future aircraft.

In addition to the S-2 aircraft, two dynamically scaled aircraft have been developed by Jordan et al.[7, 8]. These aircraft are known as the GTM-T1 and GTM-T2. These aircraft were designed to be 5.5% scaled version of an actual commercial aircraft. The GTM-T2 has a lighter airframe allowing for additional instrumentation and electronics. The aircraft moments of inertial are scaled proportionally using geometric scaling. However, the weight was increased slightly, to account for the increased lift due to the higher air density at the lower altitude at which these aircraft fly.

The weight of an aircraft's components can be estimated by a comparison of available

data for similar aircraft. Beltramo et al.[9] used this method to generate an estimation of the component weights for a commercial aircraft. It was found that the takeoff weight was sufficient for estimating the weight of the aircraft's wing.

2.1 Aerodynamics

The effect of wing tip loss and aileron loss on the aircraft's aerodynamic stability derivatives with static aeroelastic effects was explored by Woo[10]. A detailed finite element model of the wing structure was coupled to a doublet lattice model for a fighter type aircraft. For the investigated damage cases, the introduction of a rolling moment coefficient due to pitch was the most significant effect of damage. Also there was significant pitch/yaw coupling.

Render et al.[11] used windtunnel tests to study the aerodynamic effects of a hole in a wing. This type of damage created two different flow patterns referred to as a weak-jet and a strong-jet. For the weak-jet the flow remained attached, and the hole had little effect on the overall aerodynamic loads. When the flow through the hole did not remain attached it formed a strong-jet pattern which has a larger effect on the aerodynamic loads. The damage caused an increase in the drag that was most significant for a hole near the trailing edge. A decrease in the lift was shown to increase as the damage moved forward.

The GTM has been the subject of extensive windtunnel tests for the exploration of LOC events. The initial tests by Foster et al.[12] focused on the aerodynamics at very large angles of attack, $-5°$ to $85°$, and sideslip, $-45°$ to $45°$. Existing techniques used for fighter aircraft have been used as a basis for these studies. The tests included static, rotary balance, and forced oscillation tests. At very large angles there are hysteresis effects on the aerodynamic forces. Flow visualization was used to try to better understand the cause of these effects. However, the results were inconclusive. The time dependent effects were handled by averaging the aerodynamic forces. These tests revealed that large angles of attack can cause a loss of static stability. Furthermore, it was observed that there is a loss of rudder effectiveness at these very large angles of attack.

More recent windtunnel experiments by Shah[13] have explored the effects of damage on the GTM. These damage cases include 6 cases of wing tip loss, 3 cases of horizontal tail loss, 3 cases of vertical tail loss, and various other cases such as holes in the lifting surfaces. These tests showed that the loss of a wing tip leads to a reduction in the lift curve slope consistent with a reduction in aspect ratio. These tests also illustrated the rolling moment observed by Woo[10]. Furthermore, it was shown that the rolling moment at trim can be reduced by trimming the aircraft at a negative sideslip.

Rawlings[1] also conducted windtunnel test on the GTM to explore the use of the stabilator on the GTM as a device for recovering from a loss of control or as a speed break-brake. This work provides many details on the configuration of the GTM, specifically the travel limits for the control surfaces. These tests showed that the stabilator did not provide an appreciable benefit for the recovery after a loss of control incident. The stabilator did work well as a speed brake, but this resulted in significant loads on the stabilator limiting its usefulness.

The investigation of asymmetric flight has not been restricted to aircraft. Using lifting surface theory, Thomas[14] explored the aerodynamics of a bird with an asymmetric wing or tail. It was observed that asymmetry reduced the lift and increased the turning radius. However, this effect was less pronounced when the asymmetry was in the tail.

Aircraft upsets can introduce significant aerodynamic non-linearities. Keller et al.[15] used non-linear lifting line theory to capture these effects. The effect of the wake was modeled by a code used previously for rotorcraft. Few details of this model were provided in the present work. Comparison of this model against flight test data of a small radio controlled aircraft showed reasonable correlation.

2.2 Flight Dynamics

Trying to better define what constitutes a loss of control, Wilborn and Foster[16] defined a set of 5 quantitative metrics. These metrics include the adverse aerodynamics envelope (angle of attack and sideslip) and the structural integrity envelope (airspeed and load factor). Exceeding one of these envelopes constitutes an upset condition, which is likely recoverable. Yet as more of these envelopes were exceeded, it became increasingly difficult to recover. Once three of these limits had been exceeded, control of the aircraft had been lost.

The damage of an aircraft can cause a shift in the center of gravity, which complicates the simulation with traditional cg-centric equations of motion. Bacon and Gregory[17] were able to overcome this complication by deriving the equations of motion about an arbitrary fixed point. Using Newton's method, the equations of motion were calculated such that the offset of the center of gravity is a system parameter. This allows the location of the center of gravity to have discontinuous changes without having discontinuities in the system states. The results of these new equations are demonstrated against traditional cg-centric equations. These two methods yield equivalent results. Nevertheless, the new method presents the advantage of significantly simpler implementation.

The work of Nguyen et al.[18, 19] used similar equations. However, the original equations of motion do not correctly model the change in the center of gravity but were corrected in a later erratum[20]. To account for the effects of damage, the trim was considered with either a non-zero roll angle or a non-zero sideslip angle. Using a finite differencing approach, the trim was calculated with respect to the undamaged aircraft's trim. This model used the linear stability derivatives from a vortex lattice model of the GTM to capture the aerodynamic effects. The resulting flight dynamics model was used to demonstrate an adaptive control scheme base on dynamic inversion. Indirect control was achieved by a neural network or recursive least squares to update the baseline dynamic inversion law. In addition, a direct controller was used to enhance the performance.

Liu et al.[21] examined the flight dynamics of a damaged aircraft with the goal of im-

plementing a model reference adaptive controller (MRAC). This work focused on a linear model of the aircraft, using a linearized form of the equations of motion from Bacon and Gregory[17]. It was shown for three input-output cases that the system was minimum phase and the damage had no effect on the zero dynamics or the relative degree. There was an effect on the sign of the transfer function gain. A model reference adaptive controller was then demonstrated that is able to account for these changes.

Sarigul-Klijn et al.[22] also explored the effects of wing tip loss on the flight dynamics. A set of analytical corrections was developed to adjust the undamaged aircraft's stability derivatives to model the wing tip loss. These methods considered the reduction in the wing area and the reduction in the aspect ratio. However, the coupling introduced is limited to the rolling moment due to an angle of attack. As with the previous work, the equations of motion were derived about an arbitrary fixed point.

The region of attraction and the reachability of the longitudinal dynamics of the undamaged GTM was examined by Pandita et al.[23]. The non-linear equations were used to generate a polynomial model of the longitudinal dynamics to allow an analytical solution. Since Lyapunov's direct method is a sufficient condition for stability, a quadratic Lyapunov equation was used to establish a lower bound for the region of attraction. To determine an upper bound, direct Monte Carlo simulations were used.

2.3 Structural Loads

Kier and Looye[24] generated a time domain simulation of the gust and maneuver loads on an undamaged conventional aircraft. The aerodynamics were modeled using a doublet lattice method (DLM). A rational function approximation (RFA) was used to translate the frequency domain DLM data into the time domain. This model was used to show the loads due to a discrete sinusoidal gust and was verified against the frequency domain results.

Time domain simulation of the the loads on a highly flexible flying due to random gust

goals were explored by Patil[25]. The gust was modeled as a sum of sinusoids weighted to match the von Kármán gust spectrum. This random gust loading was applied to a model of the aeroelastic and flight dynamics response. This model is able to account for the geometric non-linearities due to large deformation of the aircraft's structure. Fourier transforms were used to transform the resulting time domain response into the power spectrum density. This allowed comparison to the analytical frequency domain calculation. These two models show good correlation. However, the time domain approach allows for the consideration of non-linear effects that can be caused by larger gusts.

High fidelity methods were used by Raveh[26] to model the the loads on an undamaged fighter aircraft during steady maneuvers, such as a pull-up. This aircraft had redundant control surfaces, similar to the active aeroelastic wing aircraft. To provide a unique trim, the controls were selected such that they minimized the root bending moment. A strongly coupled CFD and finite element method was used to decrease computational time. Yet this approach required 2 to 12 hours and gives the loads only for a single operational point in time.

Convers et al.[27] explored the effects of a hole in the aircraft wing on the flutter boundary. The wing was modeled as a cantilevered rectangular plate. A theoretical model of this plate was developed by coupling a finite element model and the aerodynamic forcing from a doublet lattice method. The flutter speed and frequency were found using the k-method. The use of the linear doublet lattice method does restrict the flow to the weak-jet described by Render et al.[11]. Despite this limitation, there was good matching between the experimental and theoretical models. It was observed that the hole slightly increased the flutter speed and decreased the flutter frequency. This effect was more pronounced for a hole near the wing tip.

The structural load control for a damaged aircraft was explored by Smith et al.[28]. This analysis was restricted to the debonding of the wing skin panels. Strain measurements of the wing skin are compared against an a priori model of the undamaged wing. Debonding of the wing skin will cause a reduction in the strains. This triggers a system identification by

recursive least squares with exponential forgetting. This system identification can be coupled with an adaptive controller that will prevent the buckling of the weakened wing.

Chapter 3

Modeling of Flight Mechanics

The first objective of the present work is the be able to model the motion of a damaged aircraft. This requires consideration of the effect of damage on the aerodynamics and the inertial properties.

Several coordinate systems are used to represent the aircraft's motion and the forces on the aircraft. The body axis, stability axis, and wind axis are shown in Figure 3.1b. The origin of the body axis is fixed at the location of undamaged aircraft's center of gravity. The body axis x-direction is aligned parallel to the centerline of the fuselage, and the x-z plane is coplanar with the plane of symmetry of the undamaged airplane. The origin of the stability axis is coincident with the origin of the body axis, but it is oriented such that the relative wind lies in the x-y plane. These coordinate systems are related to an inertial coordinate system as shown in Figure 3.1a. The final coordinate system used is the local structural axis. The local axis system is described in further detail in 4.

The superscripts on vectors describe the vector's coordinate system. The first letter of the superscript on a vector describes the point of interest. The parameter after the slash describes the frame of reference. For example, $\left\{\mathbf{v}^{L/B}\right\}$ is the velocity of the origin of the local axis system in the body axis directions. If the second parameter is omitted, then the frame of reference is implied to be the same.

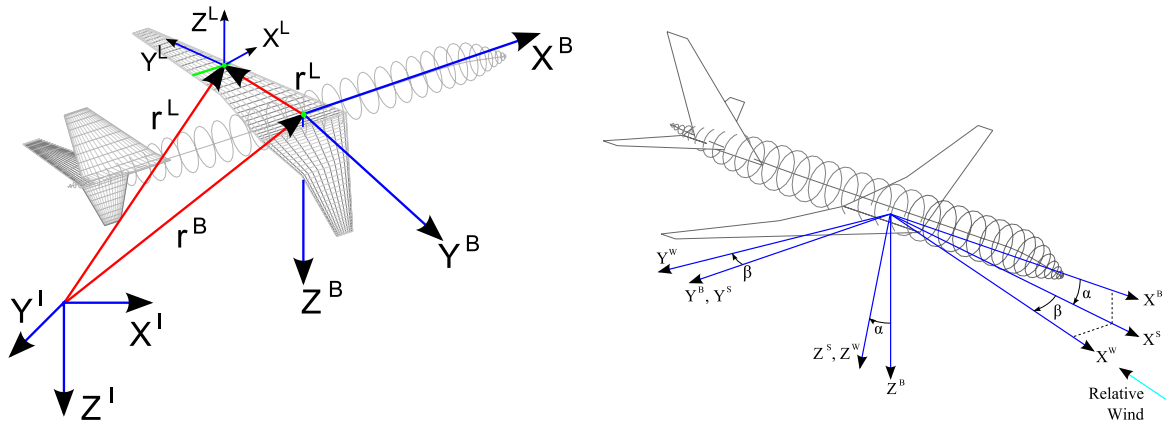

(a) Inertial, body, and structural axis systems (b) Body, stability, and wind axis systems

Figure 3.1: Definition of aircraft axis systems

3.1 Equations of Motion

When a section of an aircraft wing is lost, it will cause an instantaneous shift in the aircraft's center of gravity. If the equations of motion are defined such that the body axis is fixed at the center of gravity, then the damage will cause an instantaneous shift in the origin of the coordinate system and a discontinuity in the system states. The discontinuity complicates the simulation of the aircraft's flight dynamics. To prevent the discontinuity, the equations of motion are derived such that the body axis is fixed at an arbitrary point of the aircraft. The location of the center of gravity, $\{\boldsymbol{\Delta}^B\}$, is thus a parameter of the aircraft. The dynamic equations of an aircraft with an arbitrary body axis are given by Bacon and Gregory[17]:

$$\begin{Bmatrix} \dot{\mathbf{v}}^B \\ \dot{\boldsymbol{\omega}}^B \end{Bmatrix} = \begin{bmatrix} m\mathbb{I}_3 & -m\widetilde{\boldsymbol{\Delta}}^B \\ m\widetilde{\boldsymbol{\Delta}}^B & \mathbf{I}^B \end{bmatrix}^{-1} \left(\begin{Bmatrix} \mathbf{F}^B \\ \mathbf{M}^B \end{Bmatrix} - \begin{bmatrix} m\widetilde{\boldsymbol{\omega}}^B & -m\widetilde{\boldsymbol{\omega}}^B\widetilde{\boldsymbol{\Delta}}^B \\ m\widetilde{\boldsymbol{\omega}}^B\widetilde{\boldsymbol{\Delta}}^B & \widetilde{\boldsymbol{\omega}}^B\mathbf{I}^B - m\widetilde{\mathbf{v}}^B\widetilde{\boldsymbol{\Delta}}^B \end{bmatrix} \begin{Bmatrix} \mathbf{v}^B \\ \boldsymbol{\omega}^B \end{Bmatrix} \right) \tag{3.1}$$

$$\left[\widetilde{\mathbf{v}}^B\right] = \begin{bmatrix} 0 & -w & v \\ w & 0 & -u \\ -v & u & 0 \end{bmatrix} \qquad \left[\widetilde{\boldsymbol{\omega}}^B\right] = \begin{bmatrix} 0 & -r & -q \\ r & 0 & -p \\ -q & p & 0 \end{bmatrix}$$

$$\left[\widetilde{\boldsymbol{\Delta}}^B\right] = \begin{bmatrix} 0 & -\Delta z & \Delta y \\ \Delta z & 0 & -\Delta x \\ -\Delta y & \Delta x & 0 \end{bmatrix} \qquad \left[\mathbf{I}^B\right] = \begin{bmatrix} I_{xx} & -I_{xy} & -I_{xz} \\ -I_{xy} & I_{yy} & -I_{yz} \\ -I_{xz} & -I_{yz} & I_{zz} \end{bmatrix}$$

One can see that if the offset of the center of gravity, $\left\{\boldsymbol{\Delta}^B\right\}$, is zero then these become the standard equations of motion of an aircraft about the center of gravity[29]. The kinematic equations remain the same for the damaged aircraft. The orientation of the aircraft in the inertial frame is described by the Euler angles[30]:

$$\begin{Bmatrix} \dot{\phi} \\ \dot{\theta} \\ \dot{\psi} \end{Bmatrix} = \begin{bmatrix} 1 & \sin\phi\tan\theta & \cos\phi\tan\theta \\ 0 & \cos\phi & \sin\phi \\ 0 & \sin\phi\sec\theta & \cos\phi\sec\theta \end{bmatrix} \left\{\boldsymbol{\omega}^B\right\} \tag{3.2}$$

These Euler angles also define the directional cosine matrix which rotates from the inertial reference frame to the body axis system.

$$\left[\boldsymbol{C}^{B/I}\right] = \begin{bmatrix} \cos\theta\cos\psi & \cos\theta\sin\psi & -\sin\theta \\ \sin\phi\sin\theta\cos\psi - \cos\phi\sin\psi & \sin\phi\sin\theta\sin\psi - \cos\phi\cos\psi & \sin\phi\cos\theta \\ \cos\phi\sin\theta\cos\psi - \sin\phi\sin\psi & \cos\phi\sin\theta\sin\psi - \sin\phi\cos\psi & \cos\phi\cos\theta \end{bmatrix} \tag{3.3}$$

The velocity of the aircraft in the inertial reference frame is then given by rotating the body axis velocity[29].

$$\left\{{}^I\dot{\mathbf{r}}^{B/I}\right\} = \left[\boldsymbol{C}^{B/I}\right]^{-1}\left\{\mathbf{v}^B\right\} \tag{3.4}$$

These velocities in the inertial frame provide the trajectory of aircraft in the inertial reference frame.

3.1.1 Trim Calculations

For the simulations it is beneficial to be able to examine the aircraft's motion about some steady state solution. These steady state solutions are represented by[30]:

$$\begin{array}{llll} \dot{u} = 0 & \dot{p} = 0 & \dot{\phi} = \text{Roll Rate} & \dot{x} = \text{Velocity} \\ \dot{v} = 0 & \dot{q} = 0 & \dot{\theta} = \text{Pull-Up Rate} & \dot{y} = 0 \\ \dot{w} = 0 & \dot{r} = 0 & \dot{\psi} = \text{Turn Rate} & \dot{z} = \text{Climb Rate} \end{array} \tag{3.5}$$

The trim is further constrained to a specified sideslip angle:

$$\beta = \text{Sideslip} \tag{3.6}$$

Several of these steady-state conditions, such as the steady pull-up or roll, are only instantaneous solutions. In contrast, an aircraft which is trimmed for a steady turn will remain at that trim. The solution of these 13 equations is given as a function of the 4 controls and the 9 states:

$$\{\mathbf{u}_{trim}\} = \left\{ \begin{array}{cccc} T & \delta_e & \delta_a & \delta_r \end{array} \right\}^T \tag{3.7}$$

$$\{\mathbf{x}_{trim}\} = \left\{ \begin{array}{ccccccccc} u & v & w & p & q & r & \phi & \theta & \psi \end{array} \right\}^T \tag{3.8}$$

The resulting trim solution is determined using the Newton–Raphson method. Although the altitude does not appear explicitly in any of these equations, it will have an effect due to the variation in the atmospheric pressure.

The aircraft equations of motion are linearized at the trim condition. Using Lyapunov's indirect method the local non-linear stability is determined by the eigenvalues of the linearized system[31]. Each of these eigenvalues represents a linear mode of the system and can be

written as a second order system of the form[32]:

$$\ddot{x} + 2\zeta\omega\dot{x} + \omega^2 x = 0 \tag{3.9}$$

If the pole lies along the real axis the damping is $\zeta = 1$, and the response of the mode is is given by the first order system:

$$\dot{x} + \zeta\omega x = 0 \tag{3.10}$$

Plotting of the frequency and damping can provide a more direct interpretation of the transience of the system then plotting the eigenvalues in the complex plane. The eigenvectors of the linearized model are also used to examine the effect of the damage on the aircraft's response, such as coupling.

3.2 Modeling of Inertial and Gravitational Forces

For the present work the mass distribution was unavailable. To create an estimate of the distribution, an estimate for the weight of the complete wing is needed. Beltramo et al.[9] compared the weight of several conventional aircraft wings. It was shown that the weight of the wing of a commercial aircraft is strongly correlated to the aircraft's take-off weight. Thus, the wing weight in pounds is estimated by:

$$W_{wing} = 0.112 W_{TO} - 1720 \tag{3.11}$$

To be able to estimate the distribution, the mass per unit span is assumed to be proportional to the square of the chord of the wing and uniformly distributed in the cross section. The mass per unit span is given by:

$$\frac{dm_{wing}}{dy} = m' c(y)^2 \tag{3.12}$$

The unknown constant, m', is calculated from the integral:

$$m_{wing} = \int m' c(y)^2 dy \tag{3.13}$$

To determine the change in the location of the center of gravity, the aircraft's mass, and the aircraft's inertia matrix it is first necessary to determine the properties of the lost section. Since the total inertia of the wing tip is much smaller than the aircraft, the tip is treated as a point mass. Therefore, the inertia matrix is zero and the tip properties are given by:

$$m_{tip} = 2m' \int_{tip} c(y)^2 dy \tag{3.14}$$

$$\{\mathbf{r}_{cg}\} = \frac{1}{m_{tip}} \int_{tip} \{\mathbf{r}\}\, dm \tag{3.15}$$

The shift in the complete aircraft's center of gravity is then given by:

$$\{\mathbf{\Delta}_{dmg}\} = \frac{m\{\mathbf{\Delta}\} - m_{tip}\{\mathbf{r}_{cg}\}}{m_{dmg}} \tag{3.16}$$

Since the wing tip is a point mass, the effect on the aircraft's inertia matrix is given by the parallel axis theorem[33]:

$$[\mathbf{I}_{dmg}] = [\mathbf{I}] - m_{tip}\left(\{\mathbf{r}_{cg}\}^T \{\mathbf{r}_{cg}\} [\mathbb{I}_3] - \{\mathbf{r}_{cg}\} \{\mathbf{r}_{cg}\}^T\right) \tag{3.17}$$

3.3 Modeling of Aerodynamic Forces

3.3.1 Numerical Simulation of the Aerodynamic Forces

To capture the 3D effects of damage, the extended vortex lattice code Athena Vortex Lattice (AVL) is used to determine the aerodynamic loads. For the present work these forces were calculated in the body axis directions. AVL includes the effects of viscous forces, flow around

$0 \leq M \leq 0.6$	$-5^\circ \leq \alpha \leq 10^\circ$	$-7^\circ \leq \beta \leq 7^\circ$
$-0.1 \leq \hat{p} \leq 0.1$	$-0.005 \leq \hat{q} \leq 0.005$	$-0.05 \leq \hat{r} \leq 0.05$

Table 3.1: Limits on aerodynamic states for AVL simulation

slender bodies, wing thickness, camber, and compressible subsonic flow[34]. Additional details of the capabilities of AVL are provided in Appendix B.

Since AVL is based on a linear and quasi-steady vortex lattice method, there are several restrictions on the aircraft states. These restrictions on the states are given in Table 3.1. AVL is able to account for some compressibility at subsonic speeds by using the Prandtl-Glauert correction. The angle of attack and the sideslip angle are restricted such that no part of the aircraft has stalled. The point of stall is determined from the lift distribution, such that the lift coefficient along the wing remains less than the airfoil's lift coefficient at stall. AVL is a quasi-steady method and is thus able to calculate the effect of the angular velocities; $\hat{p}$, $\hat{q}$, and $\hat{r}$. However, these angular velocities must remain small[34]. The forces and moments for both the undamaged and damaged cases are non-dimensionalized using the reference parameters (chord, span, etc.) from the undamaged aircraft.

3.3.2 Reduced-Order Model of the Aerodynamic Forces

To improve the computational speed, a reduced-order model of the aerodynamics is used. This model is a set of non-dimensional coefficients ($[\mathbf{C}]$) which relate the rigid-body motion and control deflections to the aerodynamic forces. The resulting reduced-order model is of the form:

$$\begin{Bmatrix} \mathbf{F}^B \\ \mathbf{M}^B \end{Bmatrix} = \bar{q}S\,[\mathbf{C}] \begin{Bmatrix} \mathbf{v}^S \\ \boldsymbol{\omega}^B \\ \boldsymbol{\delta} \end{Bmatrix}_{aero} \tag{3.18}$$

Examination of the vortex lattice results demonstrates non-linearities introduced by damage and due to drag effects. The non-linearities are accounted for by introducing quadratic terms

into the state vector.

$$\left\{ \begin{array}{c} \mathbf{v}^S \\ \boldsymbol{\omega}^B \\ \boldsymbol{\delta} \end{array} \right\}_{aero} = \left\{ \begin{array}{ccccccccccccccc} 1 & \alpha & \frac{\alpha^2}{2} & \beta & \frac{\beta^2}{2} & \hat{p} & \frac{\hat{p}^2}{2} & \hat{q} & \frac{\hat{q}^2}{2} & \hat{r} & \frac{\hat{r}^2}{2} & \delta_a & \frac{\delta_a^2}{2} & \delta_e & \frac{\delta_e^2}{2} & \delta_r & \frac{\delta_r^2}{2} \end{array} \right\}^T \tag{3.19}$$

If only linear terms are used, then [**C**] is the linear stability derivatives used previously by Nguyen et al.[18, 19, 20] and by Sarigul-Klijn[22].

The first row of the coefficient matrix is given by the aerodynamics loads where all the states are equal to zero ($\alpha = 0$, $\beta = 0$, etc.). The remaining coefficients are calculated by linear least squares.

The AVL results provide more information than is currently available from experimental data. Thus a set of correction factors is calculated to make the ROM better match the available experimental data. To determine the correction factors, the ROM is first determined for both the AVL results and the experimental data. By comparing the two reduced-order models, a correction factor is calculated for each term in the coefficient matrix, [**C**].

$$K_{ij} = \frac{(C_{exp})_{ij}}{(C_{avl})_{ij}} \tag{3.20}$$

Several of the coefficients are approximately zero when looking at the complete aircraft. If $(C_{avl})_{ij} \approx 0$ it will cause an artificially large correction factor. If $(C_{exp})_{ij} \approx 0$ it will drive the correction factor to zero. To ensure that the correction factor does not cancel or over-inflate the coefficients, if either of the coefficients are very small ($< 10^{-5}$) the correction factor is assumed to be one.

Chapter 4

Modeling of Structural Loads

The forces acting on the aircraft's structure are due to structural, propulsive, inertial, gravitational, and aerodynamic forces. d'Alembert's principle shows that if the inertial forces are treated as an applied load to the structure, then the equilibrium equations become[33]:

$$\{\mathbf{F}\} = 0 \tag{4.1}$$

$$\{\mathbf{M}\} = 0 \tag{4.2}$$

Thus the structural loads are given by the summation of the propulsive, inertial, gravitational, and aerodynamic forces.

The aerodynamic and inertial forces are distributed loads. To determine the distribution of the moments, these forces must be integrated. AVL calculates the forces and moments per unit span at discrete points. The integration of these loads to give the moments in the body axis is given by:

$$\{\mathbf{M}^{L/B}\} \approx \left\{\mathbf{M}_0^{L/B}\right\} + \sum_{i=1}^{n}\left[\Delta l_i\left(\left\{\frac{d}{ds}\mathbf{M}^{L/B}\right\}_i + \{\mathbf{r}^{L/B}\}_i \times \left\{\frac{d}{ds}\mathbf{F}^{L/B}\right\}_i\right)\right] \tag{4.3}$$

These moments are rotated into a local structural axis to separating the bending and torsion. The y-axis of this local coordinate system is defined to point from the wing root the the tip

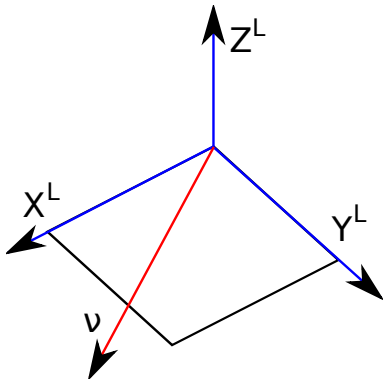

Figure 4.1: Definition of Local Structural Axis System

along the quarter chord line. The vector $\{\boldsymbol{\nu}\}$ defines the x-y plane, as shown in Figure 4.1. To provide continuity of the bending moment distribution, the vector $\{\boldsymbol{\nu}\}$ is defined:

$$\left\{\boldsymbol{\nu}^{L/B}\right\} = \left\{ \begin{array}{ccc} 1 & 0 & 0 \end{array} \right\} \tag{4.4}$$

The normal vector in the z-direction of this local coordinate system in the body reference frame is given by the cross product:

$$\hat{\mathbf{z}}^{L/B} = \frac{\boldsymbol{\nu}^{L} \times \hat{\mathbf{y}}^{L/B}}{\|\boldsymbol{\nu}^{L} \times \hat{\mathbf{y}}^{L/B}\|} \tag{4.5}$$

To ensure that the coordinate system remains a right handed coordinate system the x-direction is defined by:

$$\hat{\mathbf{x}}^{L/B} = \hat{\mathbf{y}}^{L/B} \times \hat{\mathbf{z}}^{L/B} \tag{4.6}$$

These vectors ($\left\{\hat{\mathbf{x}}^{L/B}\right\}$, $\left\{\hat{\mathbf{y}}^{L/B}\right\}$, and $\left\{\hat{\mathbf{z}}^{L/B}\right\}$) form an orthonormal basis. As a result, these vectors are the rows of the rotation matrix from the body axis system to the local axis

system[35].

$$\left[\boldsymbol{C}^{L/B}\right] = \begin{bmatrix} \hat{\mathbf{x}}^{L/B} \\ \hat{\mathbf{y}}^{L/B} \\ \hat{\mathbf{z}}^{L/B} \end{bmatrix} \tag{4.7}$$

4.1 Inertial and Gravitational Force Distribution

To determine the inertial forces first consider the linear and angular momentum of a strip of the wing. Since the center of gravity of the section may not be coincident with the structural axis, the momentum is:

$$\left\{\mathbf{P}^{L/B}(y)\right\} = m(y)\left\{\mathbf{v}^{L/B}\right\} + m(y)\left\{\boldsymbol{\omega}^{B}\right\} \times \left(\left\{\mathbf{r}^{L/B}\right\} + \left\{\boldsymbol{\Delta}^{B}\right\}\right) \tag{4.8}$$

$$\left\{\mathbf{L}^{L/B}(y)\right\} = m(y)\left\{\boldsymbol{\Delta}(y)\right\} \times \left\{\mathbf{v}^{L/B}\right\} + \left[\mathbf{I}^{L/B}(y)\right]\left\{\boldsymbol{\omega}^{B}\right\} \tag{4.9}$$

For a point on the rigid body, the velocity can be expressed by[33]:

$$\left\{\mathbf{v}^{L/B}\right\} = \left\{\mathbf{v}^{B}\right\} + \left\{\boldsymbol{\omega}^{B}\right\} \times \left\{\mathbf{r}^{L/B}\right\} \tag{4.10}$$

The momentum is then given as a function of the rigid body states from the flight dynamics:

$$\left\{\mathbf{P}^{L/B}(y)\right\} = m(y)\left\{\mathbf{v}^{B}\right\} + m(y)\left\{\boldsymbol{\omega}^{B}\right\} \times \left(\left\{\mathbf{r}^{L/B}\right\} + \left\{\boldsymbol{\Delta}(y)\right\}\right) \tag{4.11}$$

$$\begin{aligned} \left\{\mathbf{L}^{L/B}(y)\right\} = {} & \left[\mathbf{I}^{L/B}(y)\right]\left\{\boldsymbol{\omega}^{B}\right\} + m(y)\left\{\boldsymbol{\Delta}(y)\right\} \times \left\{\mathbf{v}^{B}\right\} \\ & + m(y)\left\{\boldsymbol{\Delta}(y)\right\} \times \left(\left\{\boldsymbol{\omega}^{B}\right\} \times \left\{\mathbf{r}^{L/B}\right\}\right) \end{aligned} \tag{4.12}$$

Using Newton's and Euler's equation, the inertial forces and moments are given by[17, 20]:

$$\begin{aligned}
\left\{\mathbf{F}^{L/B}(y)\right\} &= -\frac{d}{dt}\left\{\mathbf{P}^{L/B}(y)\right\} \\
&= -\left\{\dot{\mathbf{P}}^{L/B}(y)\right\} - \left\{\boldsymbol{\omega}^{B}\right\} \times \left\{\mathbf{P}^{L/B}(y)\right\} \qquad (4.13) \\
\left\{\mathbf{M}^{L/B}(y)\right\} &= -\frac{d}{dt}\left\{\mathbf{L}^{L/B}(y)\right\} + \left\{\mathbf{v}^{B}\right\} \times \left(\left\{\boldsymbol{\Delta}(y)\right\} \times \left\{\boldsymbol{\omega}^{B}\right\}\right) \\
&= -\left\{\dot{\mathbf{L}}^{L/B}(y)\right\} - \left\{\boldsymbol{\omega}^{B}\right\} \times \left\{\mathbf{L}^{L/B}(y)\right\} \\
&\quad + \left\{\mathbf{v}^{B}\right\} \times \left(m(y)\left\{\boldsymbol{\Delta}(y)\right\} \times \left\{\boldsymbol{\omega}^{B}\right\}\right) \qquad (4.14)
\end{aligned}$$

Expanding this expression gives the total inertial forces and moments.

$$\begin{aligned}
\left\{\mathbf{F}^{L/B}(y)\right\} &= -m(y)\left[\left\{\dot{\mathbf{v}}^{B}\right\} + \left\{\boldsymbol{\omega}^{B}\right\} \times \left\{\mathbf{v}^{B}\right\} + \left\{\dot{\boldsymbol{\omega}}^{B}\right\} \times \left(\left\{\mathbf{r}^{L/B}\right\} + \left\{\boldsymbol{\Delta}(y)\right\}\right)\right. \\
&\quad \left. + \left\{\boldsymbol{\omega}^{B}\right\} \times \left(\left\{\boldsymbol{\omega}^{B}\right\} \times \left(\left\{\mathbf{r}^{L/B}\right\} + \left\{\boldsymbol{\Delta}(y)\right\}\right)\right)\right] \qquad (4.15) \\
\left\{\mathbf{M}^{L/B}(y)\right\} &= -\left[\mathbf{I}^{L/B}(y)\right]\left\{\dot{\boldsymbol{\omega}}^{B}\right\} - \left\{\boldsymbol{\omega}^{B}\right\} \times \left[\mathbf{I}^{L/B}(y)\right]\left\{\boldsymbol{\omega}^{B}\right\} \\
&\quad -m(y)\left[\left\{\boldsymbol{\Delta}(y)\right\} \times \left\{\dot{\mathbf{v}}^{B}\right\} + \left\{\boldsymbol{\omega}^{B}\right\} \times \left(\left\{\boldsymbol{\Delta}(y)\right\} \times \left\{\mathbf{v}^{B}\right\}\right)\right. \\
&\quad + \left\{\boldsymbol{\Delta}(y)\right\} \times \left(\left\{\dot{\boldsymbol{\omega}}^{B}\right\} \times \left\{\mathbf{r}^{L/B}\right\}\right) + \left\{\mathbf{v}^{B}\right\} \times \left(\left\{\boldsymbol{\Delta}(y)\right\} \times \left\{\boldsymbol{\omega}^{B}\right\}\right) \\
&\quad \left. + \left\{\boldsymbol{\omega}^{B}\right\} \times \left(\left\{\boldsymbol{\Delta}(y)\right\} \times \left(\left\{\boldsymbol{\omega}^{B}\right\} \times \left\{\mathbf{r}^{L/B}\right\}\right)\right)\right] \qquad (4.16)
\end{aligned}$$

For a structural axis coincident with the body axis ($\left\{\mathbf{r}^{L/B}\right\} = \{\mathbf{0}\}$) these equations are consistent with the equations of motion derived by Bacon and Gregory[17]. The gravitational forces are given by:

$$\begin{aligned}
\left\{\mathbf{F}^{L/B}(y)\right\} &= m(y)\left[\boldsymbol{C}^{B/I}\right]\left\{\mathbf{g}^{I}\right\} \\
\left\{\mathbf{M}^{L/B}(y)\right\} &= m(y)\left\{\boldsymbol{\Delta}(y)\right\} \times \left[\boldsymbol{C}^{B/I}\right]\left\{\mathbf{g}^{I}\right\}
\end{aligned}$$

Due to limited availability of inertial data the offset from the structural axis to the section center of gravity is currently assumed to be zero ($\left\{\boldsymbol{\Delta}(y)\right\} = \{\mathbf{0}\}$). As a result, the complete

inertial and gravitational forces become:

$$\begin{aligned}\left\{\mathbf{F}^{L/B}(y)\right\} &= -m(y)\left[\left\{\dot{\mathbf{v}}^{B}\right\}+\left\{\boldsymbol{\omega}^{B}\right\}\times\left\{\mathbf{v}^{B}\right\}+\left\{\dot{\boldsymbol{\omega}}^{B}\right\}\times\left\{\mathbf{r}^{L/B}\right\}\right. \\ &\quad \left.+\left\{\boldsymbol{\omega}^{B}\right\}\times\left(\left\{\boldsymbol{\omega}^{B}\right\}\times\left\{\mathbf{r}^{L/B}\right\}\right)-\left[\boldsymbol{C}^{B/I}\right]\left\{\mathbf{g}^{I}\right\}\right] \qquad (4.17)\\ \left\{\mathbf{M}^{L/B}(y)\right\} &= -\left[\mathbf{I}^{L/B}(y)\right]\left\{\dot{\boldsymbol{\omega}}^{B}\right\}-\left\{\boldsymbol{\omega}^{B}\right\}\times\left[\mathbf{I}^{L/B}(y)\right]\left\{\boldsymbol{\omega}^{B}\right\} \qquad (4.18)\end{aligned}$$

4.2 Aerodynamic Force Distribution

The distribution of aerodynamic forces is available from the AVL results. The reduced order model of Eq. 3.18 is calculated at several locations across the span of the wing. Unlike the integrated loads, there is no experimental data for the distributed load and thus correction factors cannot be calculated for each section. Consequently, the correction factors for the ROM from the integrated loads is used for the distributed loads as well. This will ensure consistency between the structural loads and the flight dynamics loads.

Chapter 5

Results

To examine the effects of damage on a commercial aircraft, the generic transport model (GTM) was considered. The GTM was selected for the availability of the aerodynamic data, and it has been the focus of previous work on flight mechanics[22, 18, 19, 20, 21]. The data is given as table lookups used in the GTM simulation released by NASA Langley[36]. However, it is limited to the undamaged case and the 25% wing tip loss. Additionally, there is no information on the distribution of the loads.

Since the GTM operates at a lower altitude than the full scale aircraft, there will be a higher lift at a similar speed. Thus, the GTM's weight is slightly higher than the geometrically scaled weight. The correct weight for the GTM is 49.6 lbs[8]. The scaling was applied to Eq. 3.11 to give the correct weight of the GTM's wing for the inertial distribution.

5.1 Aerodynamic Forces

The aircraft's geometry was determined by examination of a 3-view CAD drawing of the full scale aircraft[37]. These dimensions were then scaled to 5.5% to match the subscale GTM. Details on the resulting geometry are provided in Appendix A. The control deflection limits, Table 5.1, are available from the work of Rawlins[1].

Table 5.1: GTM Control Travel Limits[1]

$$-30^\circ \leq \delta_e \leq 20^\circ \quad -20^\circ \leq \delta_a \leq 20^\circ \quad -30^\circ \leq \delta_r \leq 30^\circ$$

The geometry for the vortex lattice model for the undamaged case and for an aircraft with 33% damage are shown in Figure 5.1. A total of 1460 vortex elements and 37 doublet source pairs are used to model the aircraft. The data in the GTM simulation was used to validate the AVL model.

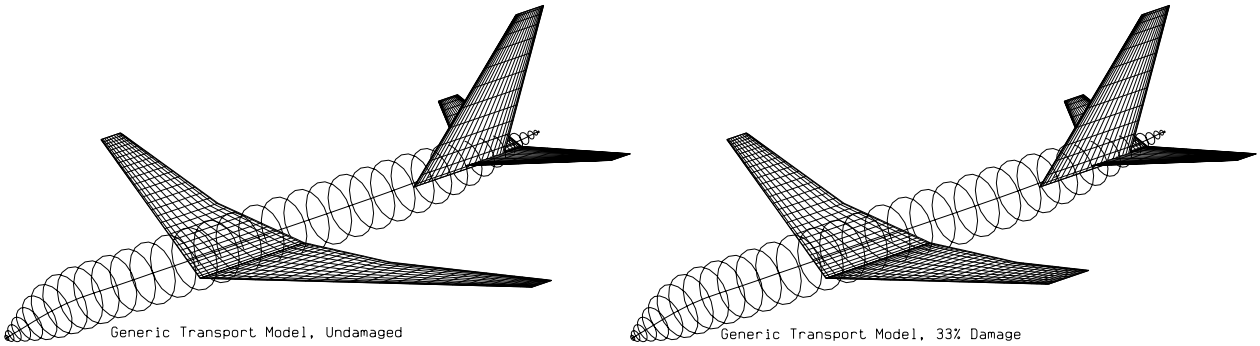

Figure 5.1: AVL Vortex Lattice Model of the GTM

5.1.1 Verification and Validation

5.1.1.1 Aerodynamics of the Undamaged Aircraft

Figure 5.2 shows the variation in the aerodynamic forces due to the change in the angle of attack. The AVL output, the data from the GTM simulation, the uncorrected reduced-order model (ROM) and the corrected ROM is shown. The GTM simulation data, which is based on windtunnel tests and has been adjusted to match parameter estimates from flight tests[36], is used to validate the AVL results. AVL is giving a good representation of the aerodynamic forces. AVL does not capture the non-linearity seen in the pitching moment, which causes a slight error. AVL also has some difficulty correctly representing the drag force. The ROM is verified by comparing the uncorrected ROM to the AVL results and the corrected ROM to the GTM simulation results. The ROM is capturing the non-linearities and matches the AVL

results very well. Furthermore, the corrected ROM matches the variation GTM simulation data. The correction factors adjust the ROM to capture the non-linearity in the pitching moment. For cases where the aerodynamic forces are zero, such as rolling moment (C_l), the correction factors are not creating singularities.

Figure 5.3 shows these models for a variation in the sideslip angle. The AVL results match the GTM data well. The corrected ROM does not adjust the C_X to match the GTM data, due to the very small coefficients. However, these coefficients are very small and the ROM still captures the variation in the GTM data quite well.

The effect of non-dimensional roll rate is shown in Figure 5.4. The AVL data does not match the GTM simulation data as well for this roll rate variation. AVL is a quasi-steady method, as a result these dynamic effects are not expected to match as well. Despite the errors in the AVL model, the corrected ROM is still matching the GTM simulation data. The effect of the pitch rate and yaw rate are shown in Figure 5.5 and Figure 5.6. For both of these cases, the AVL results match the GTM data very well. The corrected ROM is also capturing the variation shown.

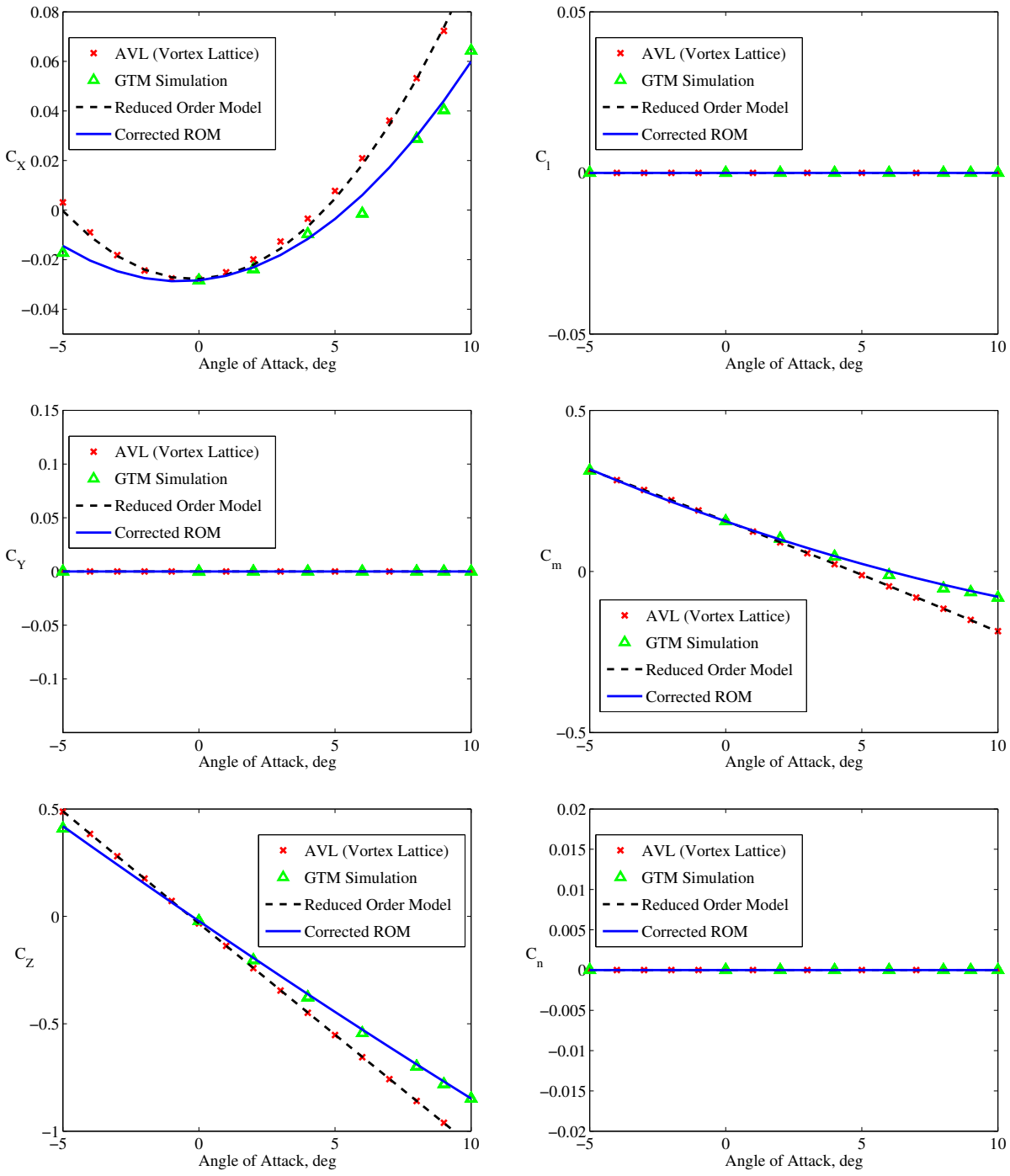

Figure 5.2: Comparison of aerodynamic data due to variation in angle of attack

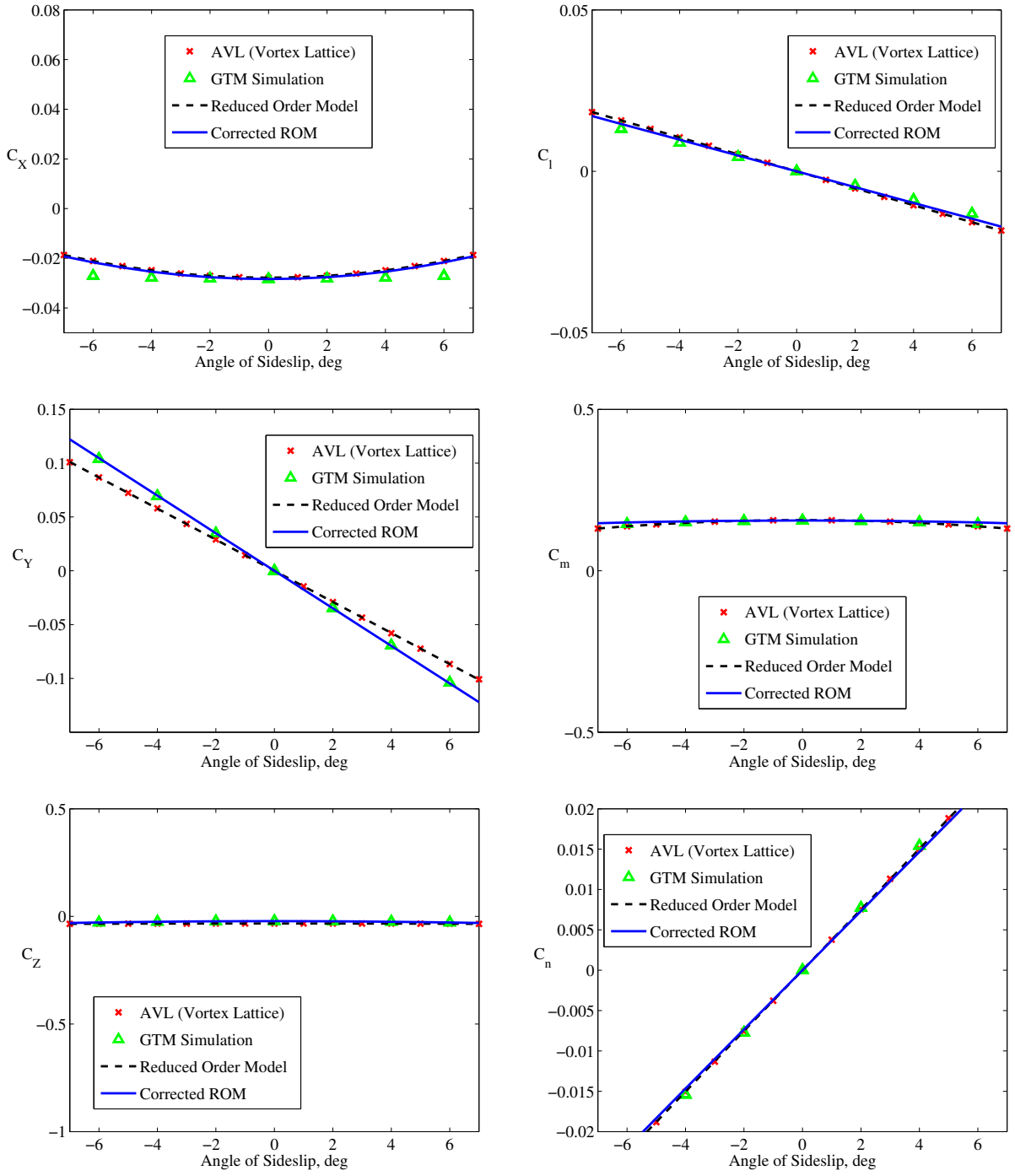

Figure 5.3: Comparison of aerodynamic data due to variation in sideslip angle

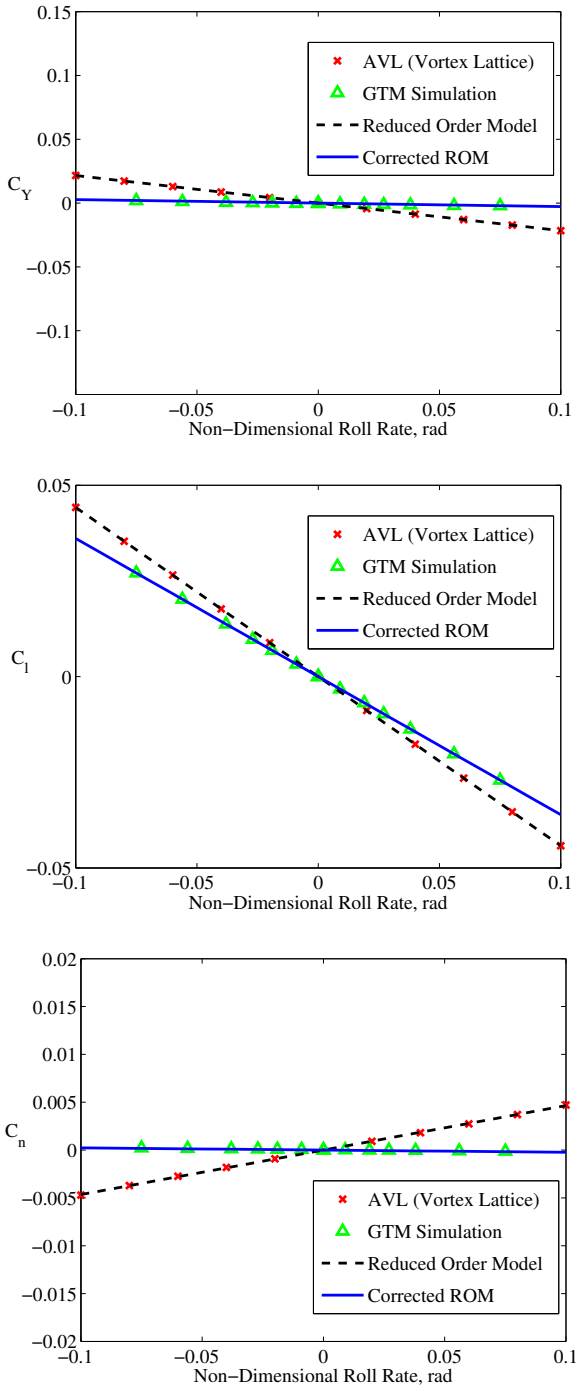

Figure 5.4: Comparison of aerodynamic data due to variation in non-dimensional roll rate

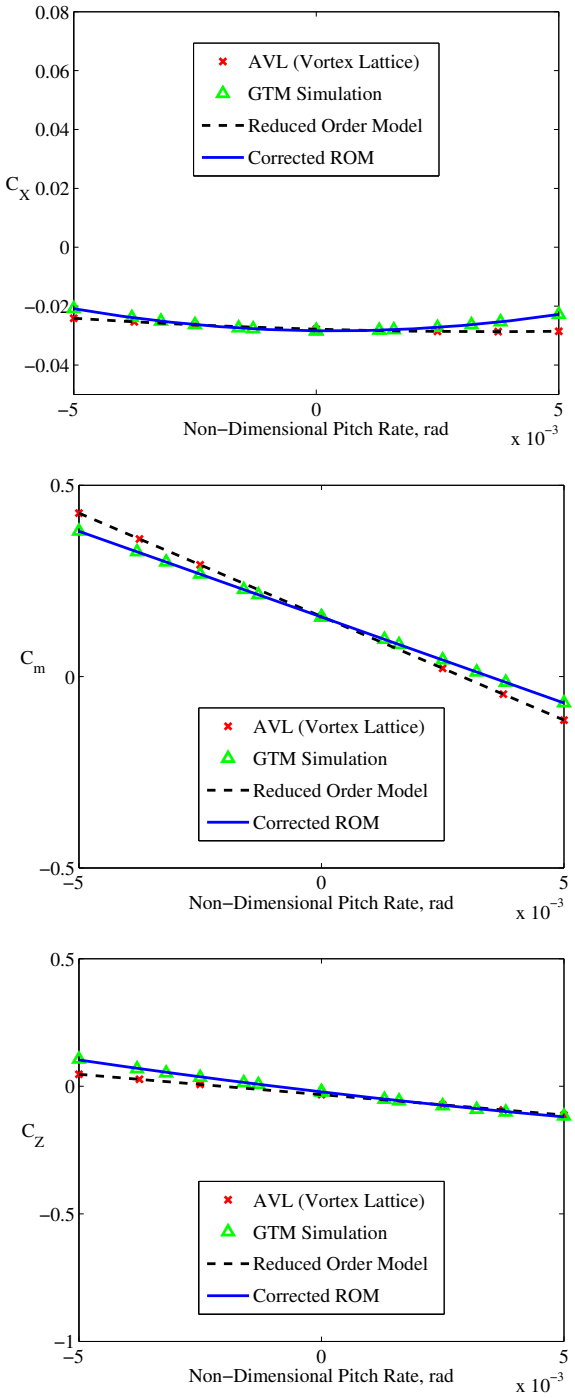

Figure 5.5: Comparison of aerodynamic data due to variation in non-dimensional pitch rate

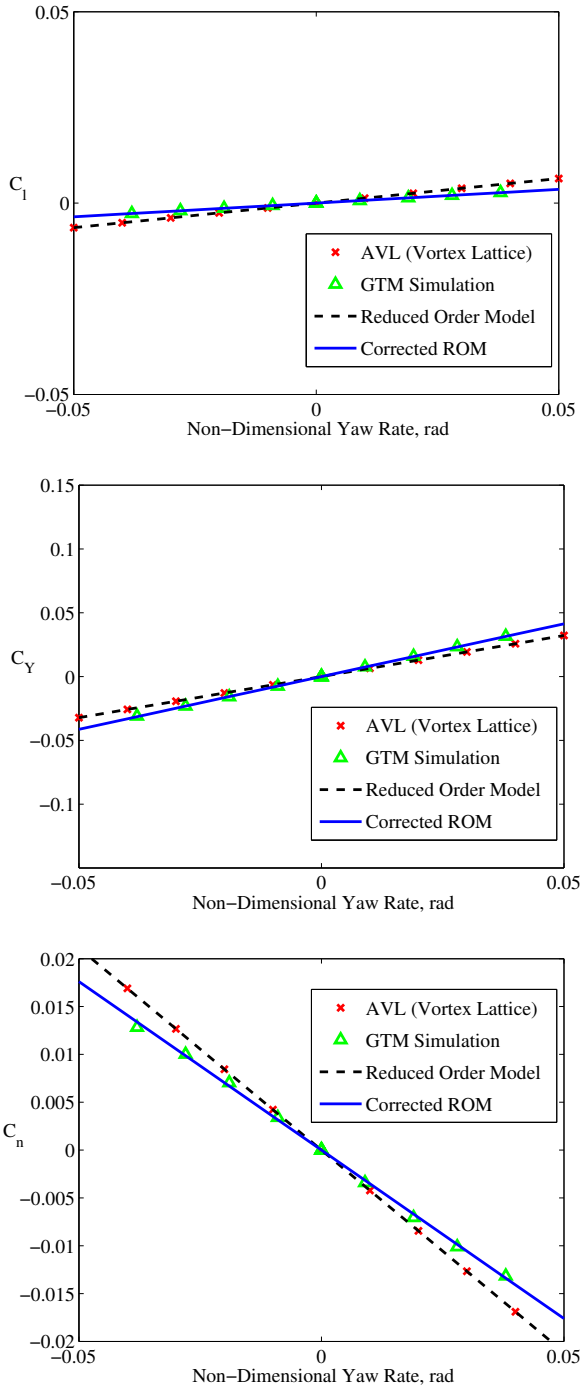

Figure 5.6: Comparison of aerodynamic data due to variation in non-dimensional yaw rate

5.1.1.2 Aerodynamics of the Damaged Aircraft

The GTM simulation does not include any information on the distribution of the forces directly. It does provide the variation of the forces with respect to the angle of attack and sideslip for the 25% damage case. Since the damage will alter the distribution of forces, this data is used to verify that the correction factors are correctly adjusting the distribution, not simply the integrated forces.

Figure 5.7 shows the variation in the aerodynamic forces with respect to the angle of attack for an aircraft with 25% damage. The corrected ROM is still matching the GTM simulation data for the longitudinal forces and moments (C_X, C_Z, and C_m), which suggests that the correction factors are correct. The undamaged aircraft has zero lateral coefficients, so the correction factor is assumed to be 1. Therefore, the corrected ROM is identical to the uncorrected ROM, but the ROM still matches the GTM data reasonably well. If this assumption is not made, then the correction factor will introduce large errors in the ROM, which could be seen in these figures.

Figure 5.8 shows the variation in the aerodynamic loads due to the sideslip angle for an aircraft with 25% tip loss. The correction factors are again correctly adjusting the distribution so that the ROM from the AVL results matches the GTM simulation data.

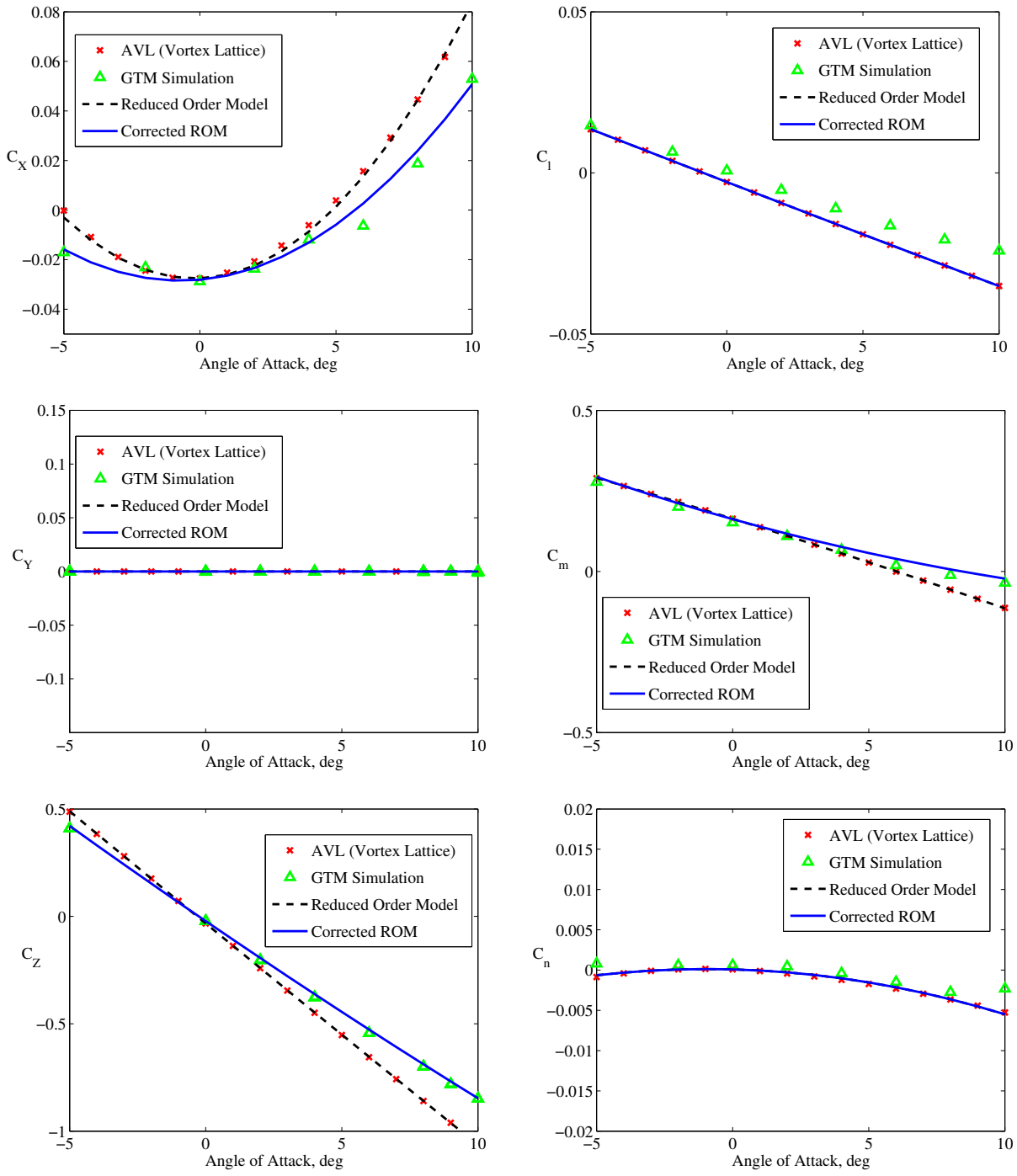

Figure 5.7: Comparison of damaged aircraft aerodynamic data due to variation in angle of attack

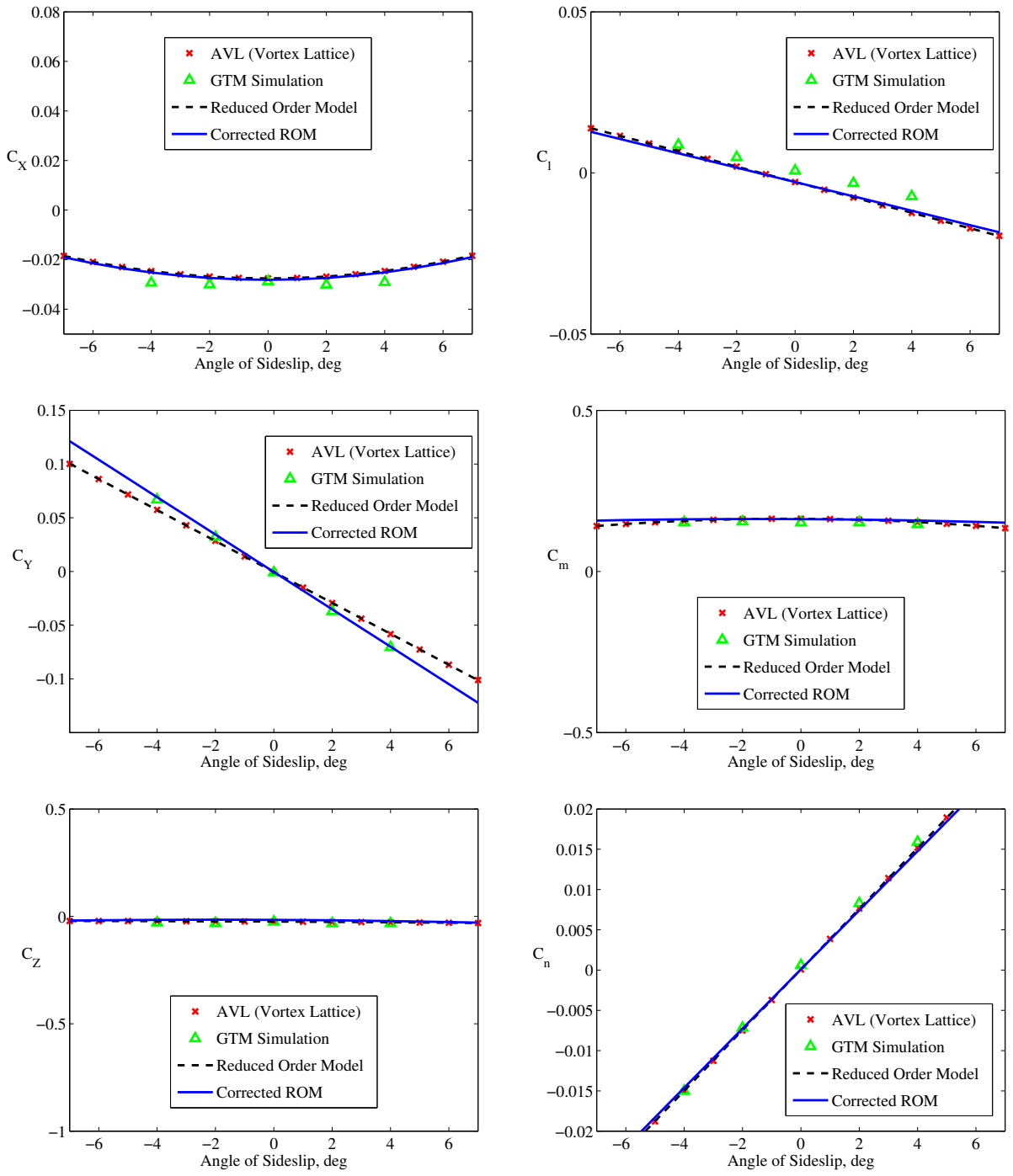

Figure 5.8: Comparison of damaged aircraft aerodynamic data due to variation in angle of sideslip

5.1.2 Vortex Lattice Results

To examine the effects of the damage on the aircraft's aerodynamics, the three forces and the three moments from the uncorrected AVL results were plotted against the five rigid body states. These are the same states used by the reduced-order model.

Figure 5.9 shows the variation in the forces and moments as the aircraft's angle of attack changes. The primary effects shown here are the change in the longitudinal force slope (C_{X_α}), vertical force slope (C_{Z_α}), and pitch stiffness (C_{m_α}) and the introduction of pitch-roll coupling (C_{l_α}) and pitch-yaw coupling (C_{n_α}). The loss of area and reduction of the aspect ratio, result in a reduction of the lift. Since the lift dominates the vertical force, there is a reduction in the vertical force slope, longitudinal force slope, and pitch stiffness. The pitch-roll coupling, which represents coupling between the longitudinal motion and the lateral motion, was introduced by the asymmetric lift distribution. The damage also introduces a non-linear variation in the yaw moment with respect to the angle of attack, due to the asymmetric drag distribution.

Looking at the variation in the forces due to sideslip angle shown in Figure 5.10, one can see the primary effect of damage was on the rolling moment (C_{l_β}). At sideslip the forward wing effectively has less sweep which results in a rolling moment. Since these wings are not symmetric after damage, the variation in rolling moment is no longer symmetric with respect to the sideslip. This effect was observed previously in the windtunnel tests by Shah[13].

For the dynamic derivatives, the aerodynamic forces are compared against the non-dimensional rates. The effect of the roll rate on the aerodynamic loads is shown in Figure 5.11. The primary effect was the reduction in roll damping (C_{l_p}) and yaw moment due to roll rate (C_{n_p}) as well as the introduction of vertical force (C_{Z_p}) and pitching moment (C_{m_p}) due to roll. Roll damping is an effect of the roll inducing an asymmetric, anti-symmetric for the undamaged aircraft, variation in the angle of attack. The reduction of lift and the reduction of the wing span results in a reduction of the roll damping. Since the effective angle of attack introduced by the roll is asymmetric for the damaged aircraft, there is a change in

the aircraft's total lift and pitching moment as a function of the roll rate. The slight effect on the yaw moment due to roll rate is a non-linear effect, again caused by the drag.

The variation of the aerodynamic loads from a pitching rate is shown in Figure 5.12. Since the effects of the pitch rate are generally dominated by the horizontal tail, which is not directly affected by the damage, these effects are small. The only significant effect seen here is the introduction of coupling between pitch rate and roll (C_{l_p}).

Similarly, the yaw rate effects are dominated by the vertical tail. Thus the nature of the variation in the forces as a function of yaw rate, shown in Figure 5.13, do not change significantly as a result of the damage.

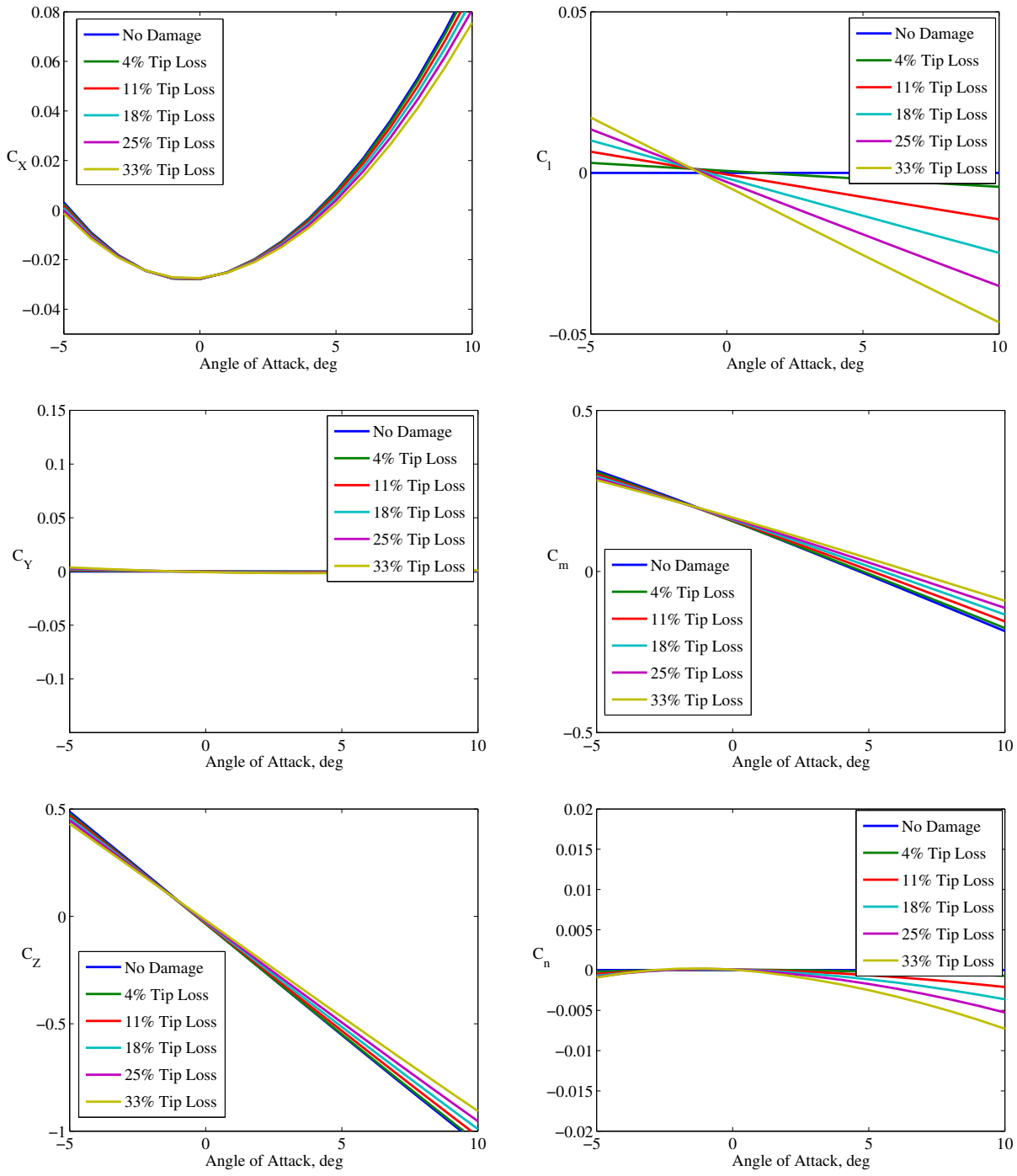

Figure 5.9: Variation in Aerodynamic Coefficients with Respect to Angle of Attack

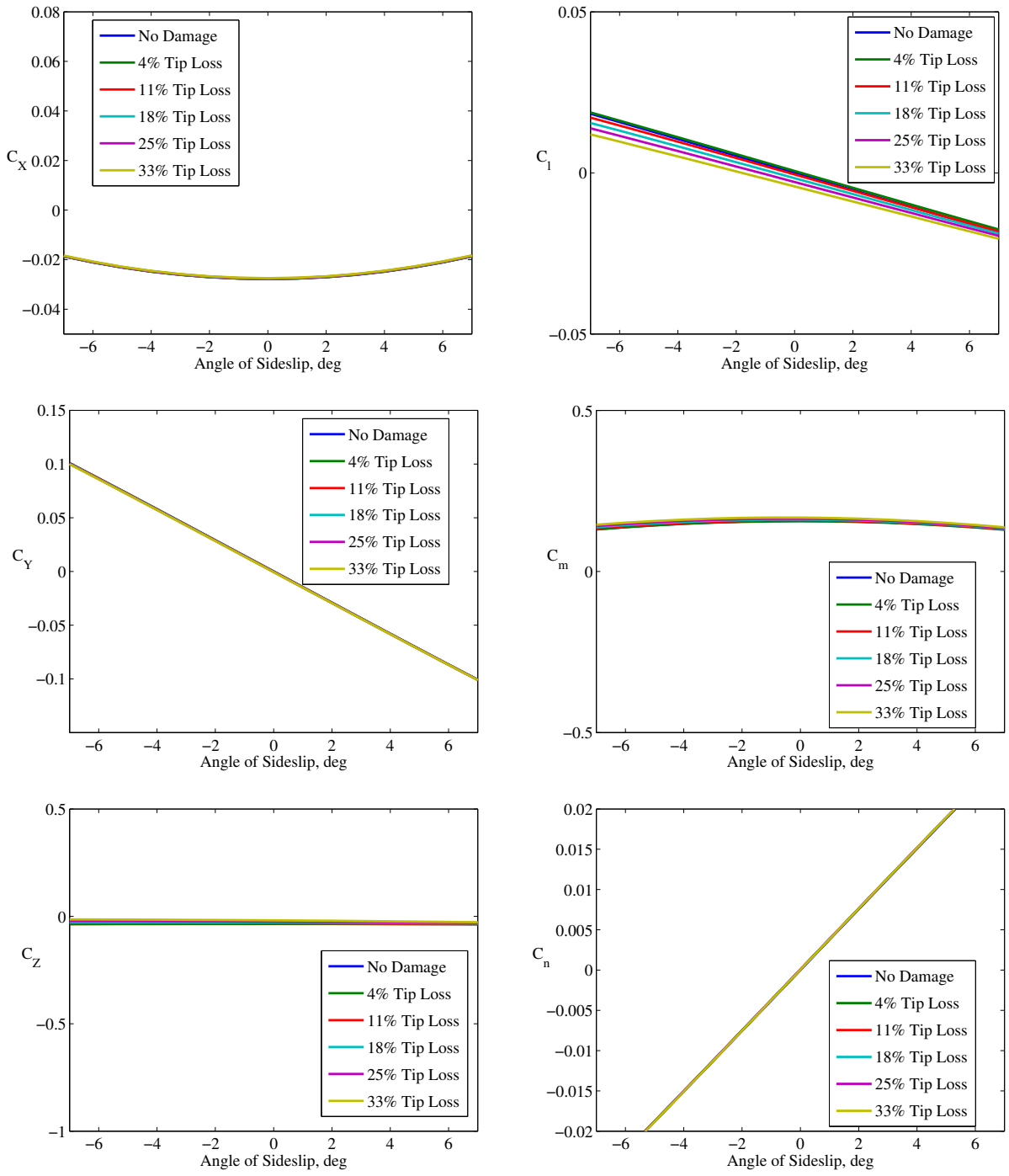

Figure 5.10: Variation in Aerodynamic Coefficients with Respect to Angle of Sideslip

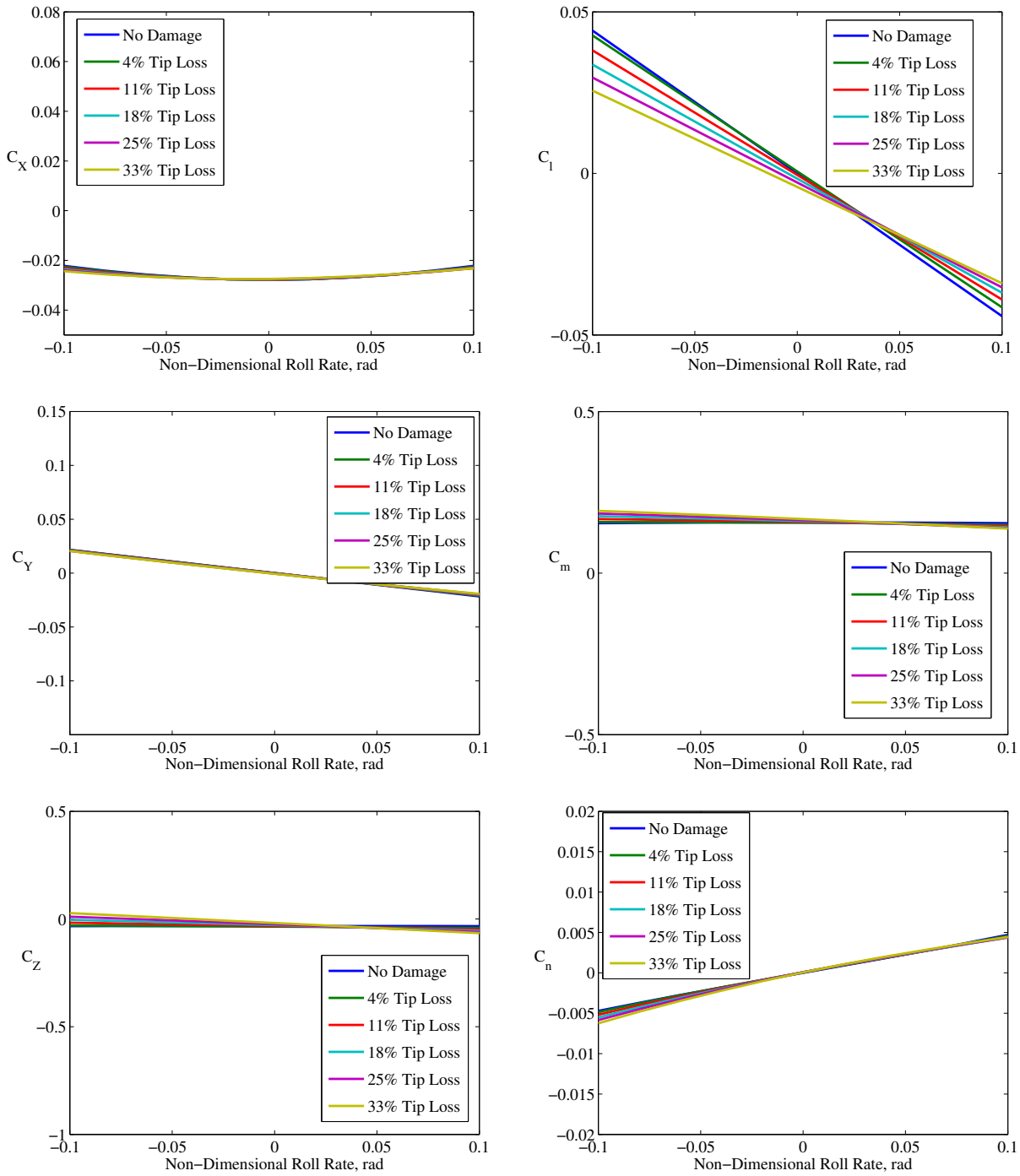

Figure 5.11: Variation in Aerodynamic Coefficients with Respect to Roll Rate

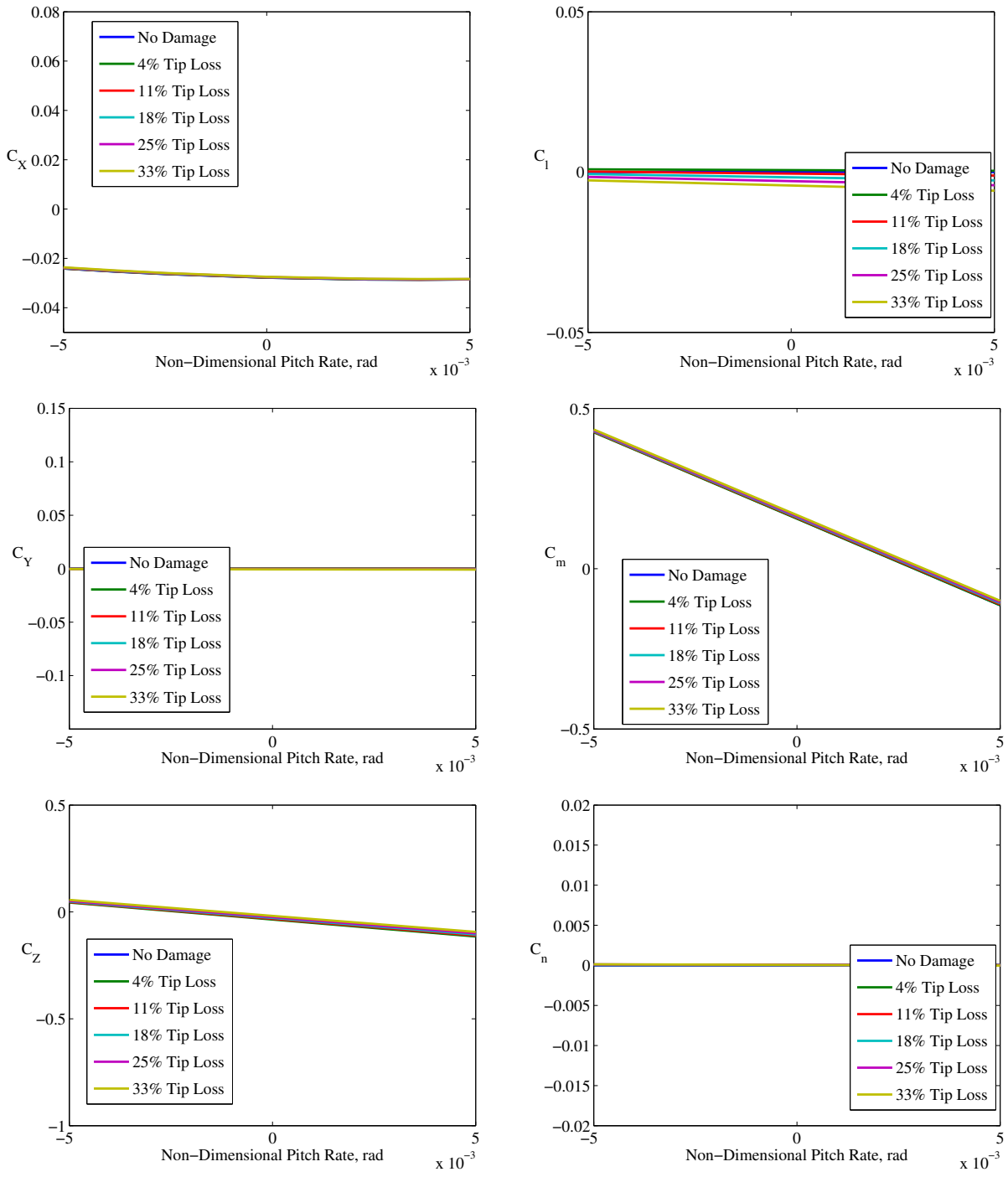

Figure 5.12: Variation in Aerodynamic Coefficients with Respect to Pitch Rate

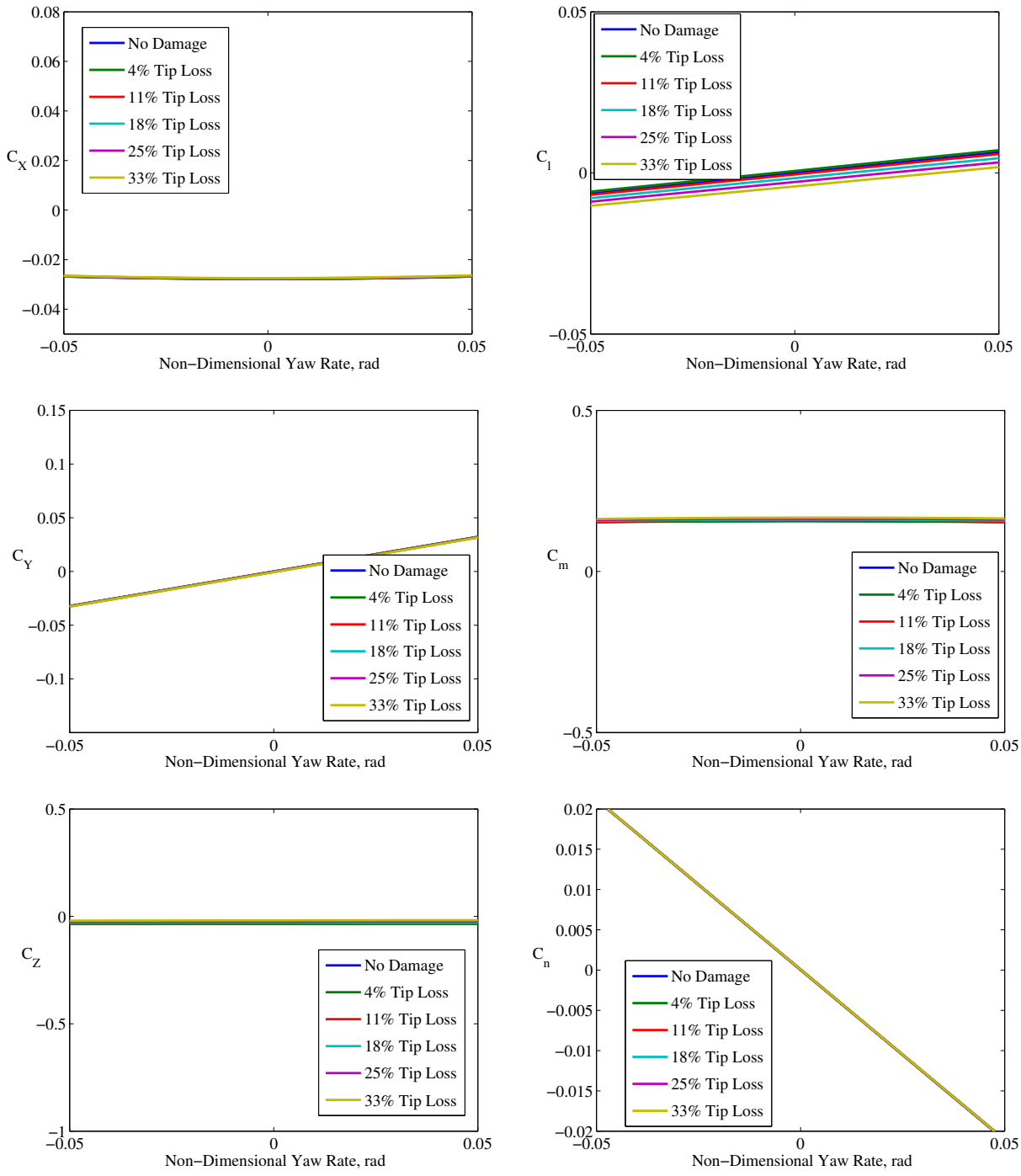

Figure 5.13: Variation in Aerodynamic Coefficients with Respect to Yaw Rate

5.1.3 Reduced-Order Model

The matrix of aerodynamic coefficients ([**C**]) for the undamaged aircraft, with the correction factors applied, is shown in Table 5.2a. Although the C_{X_r} and C_{m_r} coefficients are non-zero, they are very small and most likely due to a numerical error from the least squares. With the exception of these two coefficients, the only coupling between the lateral states and longitudinal forces is the non-linear terms. Furthermore, there is no coupling between the longitudinal states and lateral forces, resulting in the decoupling typically seen in linear models.

The aerodynamic coefficients for the aircraft with 33% wing tip loss are shown in Table 5.2b. The 33% damage case was selected because it is the maximum damage examined and will show the maximum impact on these coefficients. The damage introduces many new coupling terms. These couplings result in both the longitudinal and lateral forces being a function of all of the aircraft's states. In addition to these coupling terms, one can see the introduction of many new non-linear terms. In contrast, there is no significant effect on the effectiveness of the elevator or rudder. The change in the aileron effectiveness is due to the loss of the left aileron.

	C_X	C_Z	C_m	C_Y	C_l	C_n
$_0$	-0.0284	-0.0220	0.1556	0	0	0
α	0.0011	-0.0864	-0.0295	0	0	0
α^2	0.0015	0.0007	0.0011	0	0	0
$\hat{q}$	-0.1929	-22.2980	-44.8888	0	0	0
$\hat{q}^2$	523.0730	1085.4597	-19.7258	0	0	0
δ_e	-0.0002	-0.0075	-0.0295	0	0	0
$\delta_e{}^2$	0	-0.0001	-0.0003	0	0	0
β	0	0	0	-0.0176	-0.0024	0.0037
β^2	0	-0.0006	-0.0007	0	0	0
$\hat{p}$	0	0	0	-0.0272	-0.3609	-0.0023
$\hat{p}^2$	1.1400	-0.0779	-0.4491	0	0	0
$\hat{r}$	0.0001	0	-0.0001	0.8274	0.0717	-0.3522
$\hat{r}^2$	0.8199	-0.1518	-2.7175	0	0	0
δ_a	0	0	0	0.0003	0.0011	0
$\delta_a{}^2$	0	0	0	0	0	0
δ_r	0	0	0	0.0067	0.0006	-0.0035
$\delta_r{}^2$	0	0	0.0001	0	0	0

(a) Undamaged

	C_X	C_Z	C_m	C_Y	C_l	C_n
$_0$	0	-0.0125	0.1659	-0.0006	-0.0042	0.0001
α	0.0009	-0.0747	-0.0221	-0.0005	-0.0043	-0.0002
α^2	0.0013	0.0006	0.0009	0.0001	0	-0.0001
$\hat{q}$	-0.2037	-20.8592	-44.3569	-0.0388	-0.3222	-0.0160
$\hat{q}^2$	515.0584	-1085.4597	-19.9433	1.1059	-0.0725	-0.9065
δ_e	-0.0002	-0.0075	-0.0295	0	0	0
$\delta_e{}^2$	0	-0.0001	-0.0003	0	0	0
β	0	-0.0009	-0.0006	-0.0175	-0.0021	0.0037
β^2	0	-0.0006	-0.0007	0	0	0
$\hat{p}$	0.0066	-0.4644	-0.2741	-0.0251	-0.2433	-0.0026
$\hat{p}^2$	0.7463	-0.0736	-0.3935	0.2437	-0.0004	-0.1947
$\hat{r}$	0.0011	0.0245	0.0156	0.8254	0.0669	-0.3520
$\hat{r}^2$	0.8297	-0.1373	-2.6944	0.0009	-0.0149	-0.0016
δ_a	0	0.0023	0.0019	0.0002	0.0006	0
$\delta_a{}^2$	0	0	0	0	0	0
δ_r	0	0	0	0.0067	0.0006	-0.0035
$\delta_r{}^2$	0	0	0.0001	0	0	0

(b) 33% wing tip damage

Table 5.2: Corrected Aerodynamic Coefficients for the GTM

Table 5.3 shows the correction factors for the reduced-order model. In general the correction factors for the linear terms are close to 1 which shows a good match between the ROM from the AVL results and the GTM data. The correction factor for the $C_{Z_{\hat{q}^2}}$ term is very large, which indicates a large error in the coefficient. Yet, since the value of $\hat{q}$ is very small ($\sim 10^3$), the $C_{Z_{\hat{q}^2}}$ coefficient has a very small effect on the force (C_Z) . Therefore, the error in the coefficient does not present a significant error in the final results. The results in Figure 5.5 show how small this effect is.

	C_X	C_Z	C_m	C_Y	C_l	C_n
$_0$	1.02	0.67	0.99	1	1	1
α	2.3	0.83	0.91	1	1	1
α^2	0.64	3.84	-2.85	1	1	1
$\hat{q}$	0.43	1.39	0.83	1	1	1
$\hat{q}^2$	4.33	1330.44	1	1	1	1
δ_e	-0.08	0.38	0.4	1	1	1
$\delta_e{}^2$	0.07	4.4	-2.07	1	1	1
β	1	1	1	1.22	0.92	0.98
β^2	-0.1	7.38	0.7	1	1	1
$\hat{p}$	1	1	1	0.13	0.82	-0.05
$\hat{p}^2$	1	1	1	1	1	1
$\hat{r}$	1	1	1	1.28	0.56	0.83
$\hat{r}^2$	1	1	1	1	1	1
δ_a	1	1	1	1.35	0.68	1
$\delta_a{}^2$	1	1	1	1	1	1
δ_r	1	1	1	0.77	0.53	0.88
$\delta_r{}^2$	0.17	0.28	0.2	1	1	1

Table 5.3: Correction Factors for Aerodynamic Coefficients for the GTM

5.2 Flight Dynamics

The effect of the damage on the flight dynamics is the topic of this subsection. The focus is on an aircraft which is initially trimmed at either a level trim or a coordinated turn. For each of these trim conditions, the stability was examined and various time-marching simulations were performed. For all of the present cases the GTM is taken to be initially at an altitude

of 1000 ft and a velocity of 95 knots.

5.2.1 Verification and Validation

To verify the equations of motion and their implementation, the linear modes were compared to the values for the NAVION general aviation airplane published by Teper[38]. The original published parameters included the effects due to the rate of change of angle of attack, $\dot{\alpha}$, which the present simulation does not. The resulting frequency and damping is shown in Table 5.4. The eigenvalues of the current simulation match with those of Teper, indicating that the equations of motion are correct.

Table 5.4: Verification of linear response

	Current Simulation	Teper[38]
ω_{sp}	3.5547	3.5558
ζ_{sp}	0.5658	0.5659
ω_p	0.2131	0.2122
ζ_p	0.0725	0.0749

	Current Simulation	Teper[38]
$1/\tau_s$	0.0088	0.0088
$1/\tau_r$	8.2439	8.2555
ω_{dr}	2.3599	2.3591
ζ_{dr}	0.2039	0.2011

The current model was validated against NASA's GTM Simulation, which is based off experimental data and has been validated with flight test results[36]. The eigenvalues from the two simulations are shown in Table 5.5. The present model does not capture all of the coupling that the GTM simulation can, such as the effect of angle of attack on the roll rate derivatives. As a result, there are some slight differences between the two simulations. Despite the lack of coupling in the aerodynamics, the eigenvalues of the present simulation do match quite well.

Table 5.5: Validation of Linear Response Against GTM Simulation

Mode	Current Simulation	GTM Simulation[36]
Phugoid	$-4.1343 \pm 7.3718i$	$-3.8484 \pm 7.3752i$
Short-Period	$-0.0208 \pm 0.2304i$	$-0.0198 \pm 0.2386i$
Dutch-Roll	$-1.1052 \pm 7.0076i$	$-0.8215 \pm 5.8647i$
Roll	-7.0392	-7.7605
Spiral	-0.0722	-0.0533

5.2.2 Level Trim

Figure 5.14a shows the control deflections required to trim the aircraft for various damage cases. As shown previously, the damage introduces a rolling moment while at the level trim condition, which is complicated by the loss of aileron effectiveness due to the damage. As the damage increases, the aileron deflection becomes very large and will exceed the travel limits of the aircraft at approximately 20% wing tip loss.

Figure 5.14b shows the control deflections if the aircraft is trimmed at a sideslip angle of $-7°$. It was shown earlier by Shah[13] that if the aircraft is trimmed at a negative sideslip angle, then there is a reduction in the rolling moment, which will reduce the required aileron for the larger damage cases. For 33% damage the required aileron is less then 20°, the limit on the travel. In contrast, for the smaller damage cases the aileron exceeds the negative travel limit.

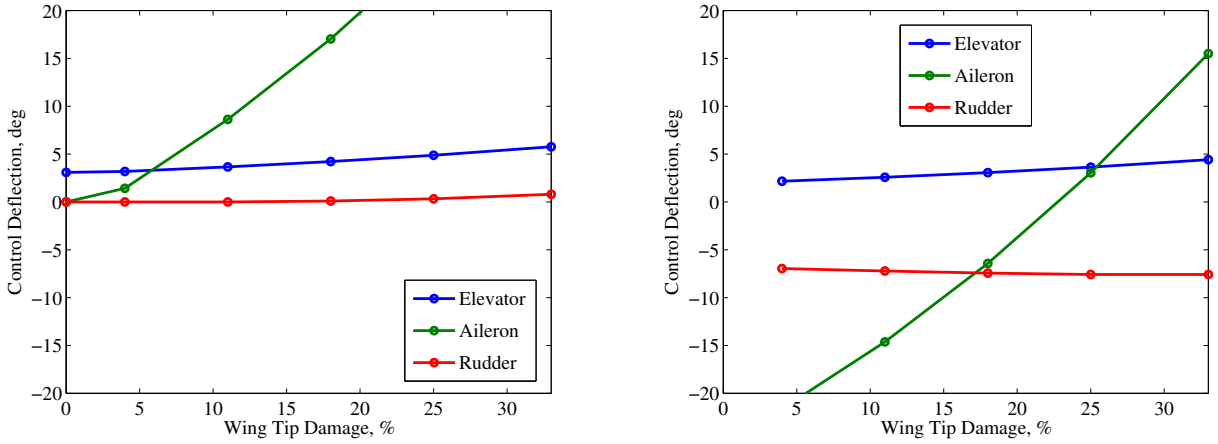

(a) Zero Sideslip

(b) Negative Sideslip ($\beta = -7°$)

Figure 5.14: Control Surface Deflection at Level Trim

Figure 5.15 shows the thrust required for an aircraft at a level trim with and without sideslip. If the aircraft is trimmed without sideslip, then the damage causes an increase in the required thrust. If the aircraft is trimmed at $-7°$ there is significantly more thrust required for small amounts of damage, but the thrust does not vary as significantly for the sideslip. As a result, for the 33% damage case the required thrust is very similar.

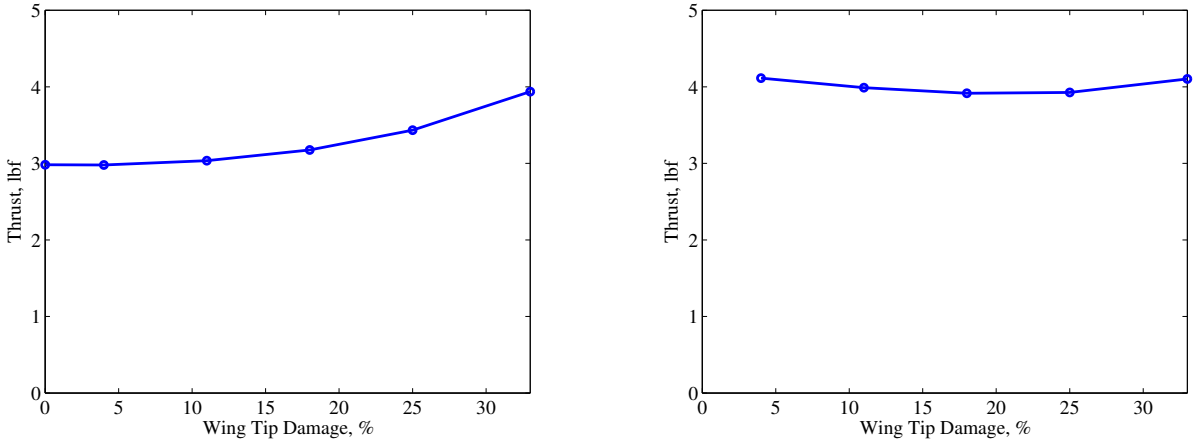

(a) Zero Sideslip

(b) Negative Sideslip ($\beta = -7°$)

Figure 5.15: Thrust at Level Trim

5.2.2.1 Stability of the Trim

Figure 5.16a shows the root locus demonstrating the change in the eigenvalues with damage. The damping is plotted increasing toward the left to make the root locus appear more consistent with the complex plane. There are three second order modes and two first order modes. The first order modes are the quick roll mode and the slow spiral mode. The second order modes consist of the high frequency moderately damped short-period mode, the high frequency and lightly damped Dutch-roll mode, and the low frequency lightly damped Phugoid mode.

Figure 5.16b shows the root locus for the aircraft trimmed at a sideslip angle of $-7°$. Again there are two first order modes and 3 second order modes. The frequency and damping of these modes is similar to the trim at zero sideslip. However, the sideslip has changed the modes such that terms such as Phugoid are no longer applicable.

For the trim at zero sideslip, the dominant effect of the damage is a slower response of the roll mode. There is also a significant reduction in the frequency and increase in the damping of the short-period mode. At zero sideslip, the damage has only a slight impact on the phugoid, the spiral, and the Dutch-roll modes. In contrast, at negative sideslip there is a reduction in the damping of the lightly damped low frequency mode. However, the ailerons reach saturation before this mode would go unstable.

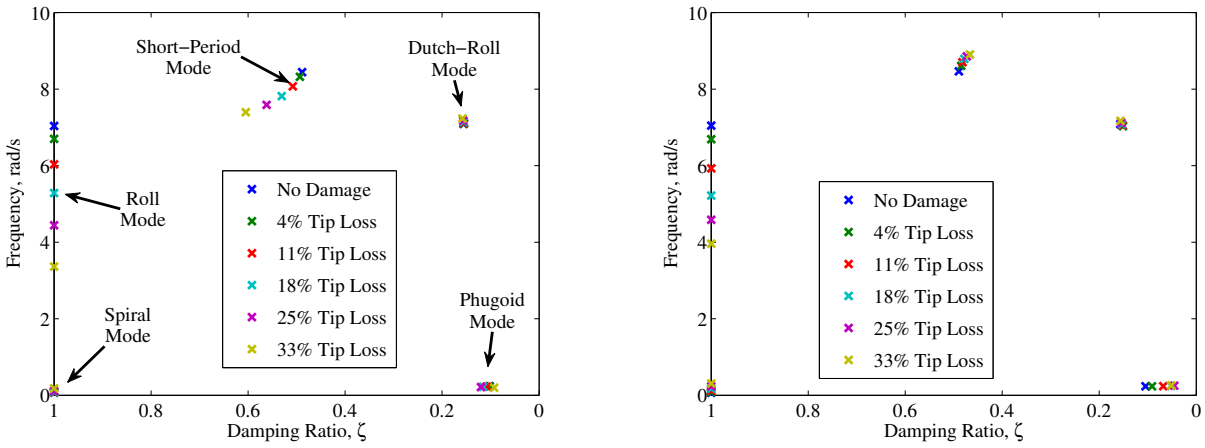

(a) Zero Sideslip

(b) Negative Sideslip ($\beta = -7°$)

Figure 5.16: Root Locus of Damaged Aircraft at Wing Level Trim

5.2.2.2 Variation in Linear Modes

The magnitude of the eigenvectors for the level trim at zero sideslip are shown in Figure 5.17. The longitudinal states are shown in blue and the lateral states are in red. For the undamaged aircraft there is a clear decoupling between these longitudinal modes and the lateral modes. Once the damage is introduced these modes are no longer decoupled.

The phugoid mode shown in Figure 5.17a is dominated by the velocity (V_T/V_{T_0}) and pitch angle (θ). The damage causes a significant increase in the roll angle (ϕ) coupling, due to the pitch-roll coupling (C_{l_α} and C_{l_q}). The short-period mode in Figure 5.17b is dominated by a variation in angle of attack (α) and pitch angle (θ). Again one can see that there is significant coupling of the roll angle (ϕ). There is also a component of the roll rate ($\hat{p}$) introduced by the damage. The Dutch-roll mode shown in Figure 5.17e, is dominated by the variation in sideslip (β) and roll angle (ϕ). The damage introduces a component of the angle of attack (α) and pitch angle (θ), but this is only a very weak coupling.

The first order modes, spiral mode and roll mode, show less significant coupling from the damage. Figure 5.17c shows the spiral mode. The spiral mode is dominated by the roll angle (ϕ). The damage does not cause any significant coupling. Figure 5.17d shows the roll mode.

The roll mode is dominated by the roll angle (ϕ) and roll rate ($\hat{p}$). The damage causes only a very slight coupling with the longitudinal states.

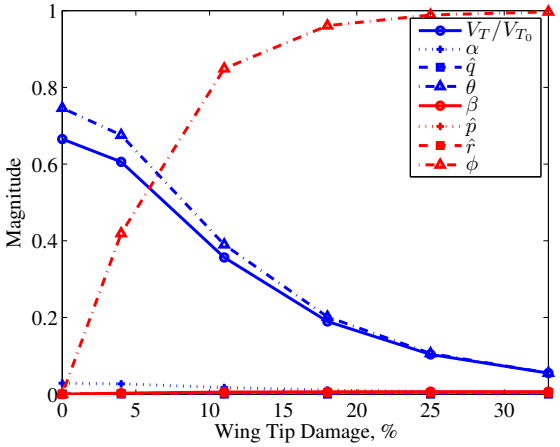

(a) Phugoid Mode

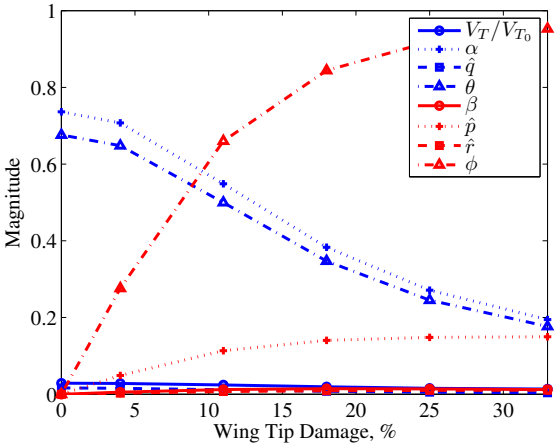

(b) Short-Period Mode

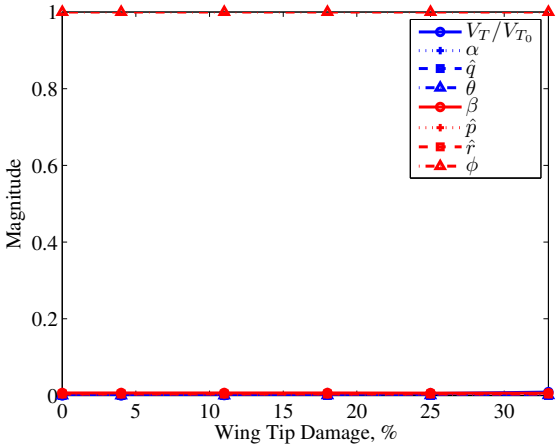

(c) Spiral Mode

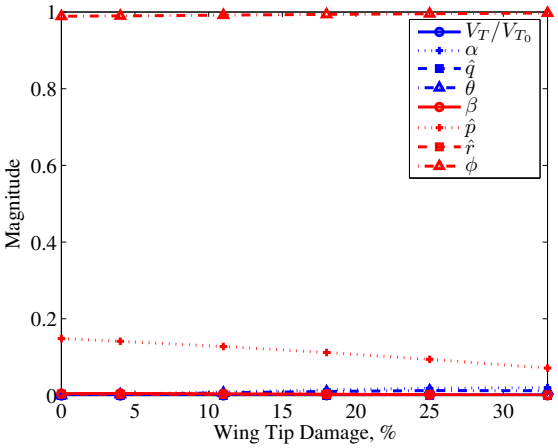

(d) Roll Mode

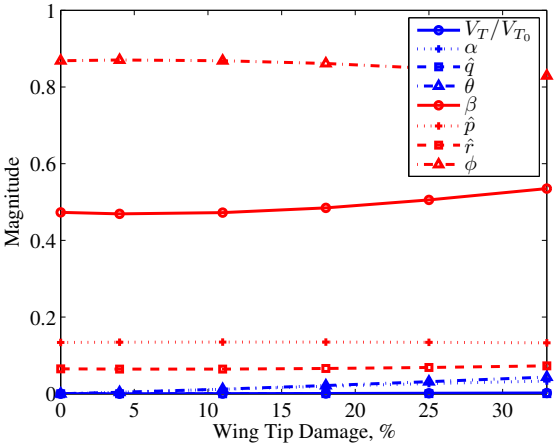

(e) Dutch-Roll Mode

Figure 5.17: Variation of Eigenvectors of Level Trim Due to Damage

5.2.2.3 Stick-Fixed Simulation

To examine the effects of the damage on the aircraft's dynamics, time-marching was used to investigate several cases. The first case is referred to as the stick-fixed simulation. For this simulation the aircraft was initially undamaged and at a level trim. After 5 seconds there was a loss of the port wing tip, without any change in the controls. The simulation was terminated when the aircraft reached an altitude of zero.

The aircraft's trajectory for the stick-fixed response is shown in Figure 5.18. Since the damage causes a reduction in lift, there is a loss altitude seen here. Additionally, the rolling moment causes the aircraft to bank left. For the small damage cases, such as 4%, the bank angle is small and the aircraft experiences a large turn. For larger damage cases the bank is much more severe. As a result the aircraft loses altitude much more rapidly.

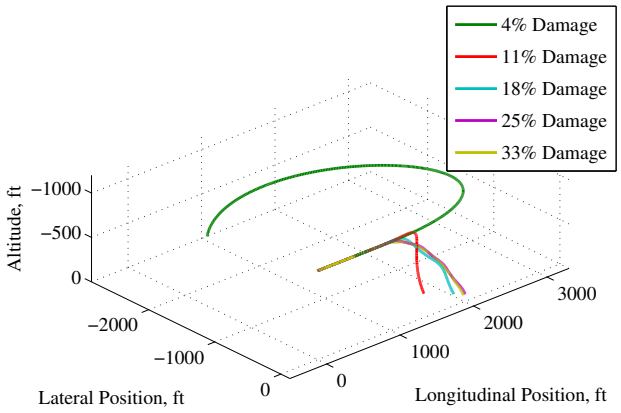

Figure 5.18: Trajectory of Stick-Fixed Response to Damage of an Initially Level Aircraft

To further illustrate this, the time history of the aircraft states is shown in Figure 5.19. The loss of altitude is converting the potential energy into kinetic energy, resulting in a divergent velocity. For 4% damage the rate of divergence is very slow but increases rapidly as the damage increases. The roll rate shows clearly the rolling motion caused by the roll coupling.

Although many of these states are very large, such as velocity and roll rate, they do not

exceed the limits imposed by the AVL aerodynamic model shown in Table 3.1. Thus the present simulation is correctly modeling the dynamics and the loads.

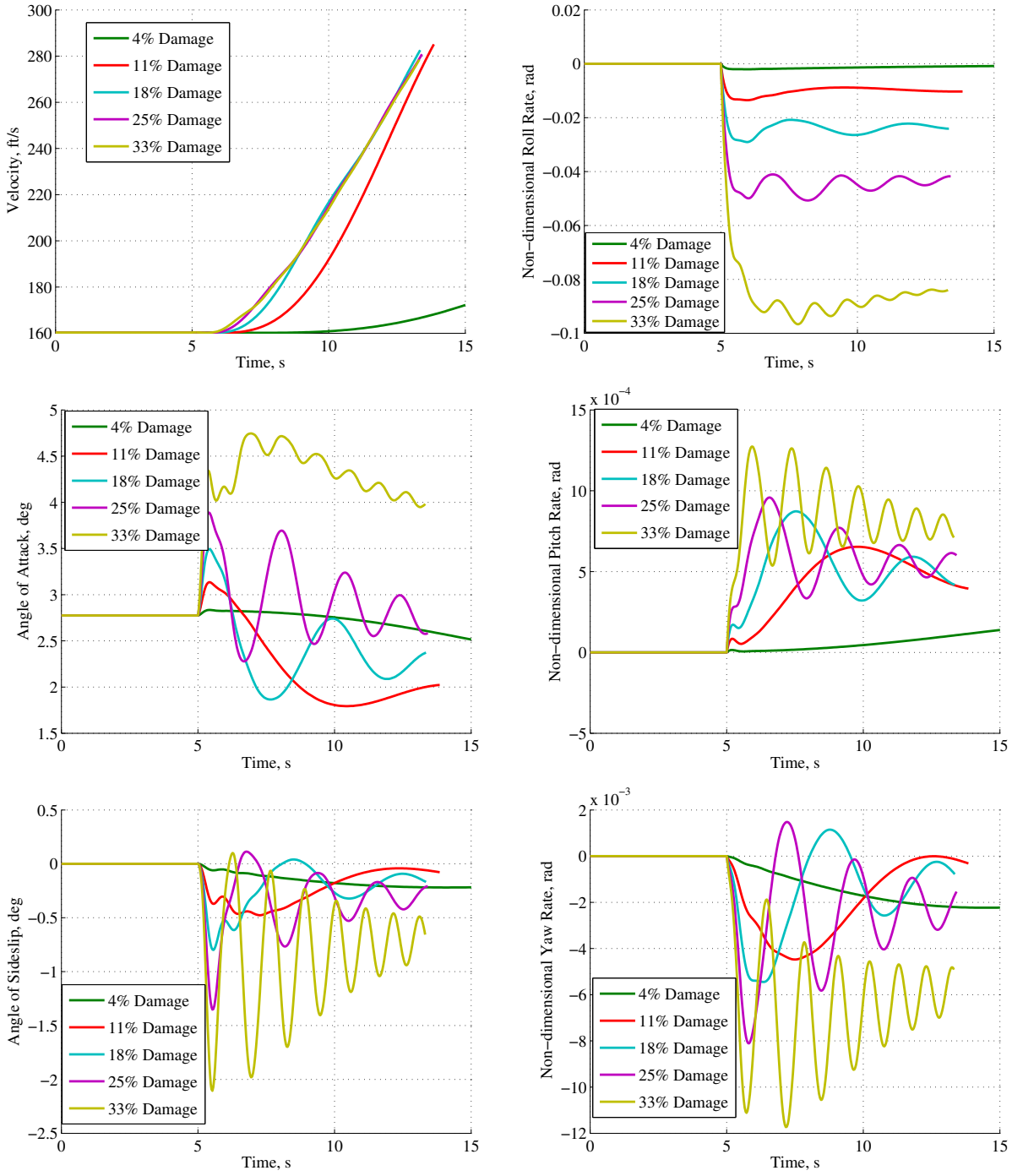

Figure 5.19: Time History of Stick-Fixed Response to Damage of an Initially Level Aircraft

5.2.2.4 Doublet Inputs

For the second simulation case, the aircraft was again taken to be initially at a level trim. To illustrate the aircraft's response to control inputs, a sequence of doublet inputs was used. The doublet sequence is shown in Figure 5.20. These doublet inputs will excite a wide band of frequencies to provide a good characterization of the system response.

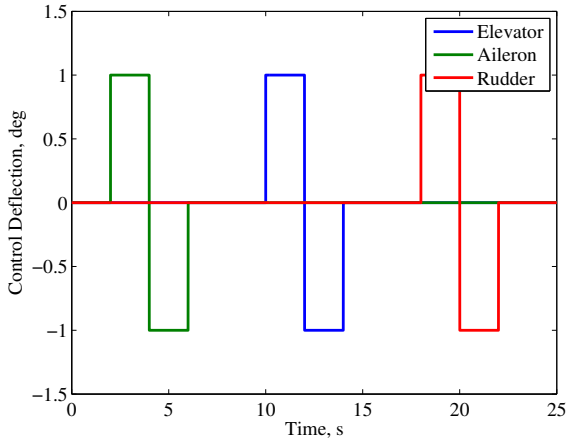

Figure 5.20: Control Doublet Input Sequence

For the first simulation, the aircraft is initially trimmed at no sideslip for each of the damage cases. The aircraft response is shown in Figure 5.21. As one would expect, the primary effect of the aileron doublet is roll rate. The elevator response causes a significant variation in angle of attack and pitch rate. The damaged aircraft also shows a significant roll rate response to the elevator doublet. This illustrates the pitch-roll coupling introduced by the damage. The rudder causes a variation in the sideslip, roll rate, and yaw rate. With the exception of the 18% damage case, the response to the rudder input does not appear to be significantly affected by the damage.

It was shown previously that the level trim condition will remain stable for 18% damage. The stability is demonstrated by the aileron input. After the aileron doublet, the aircraft does appear to be converging back to the equilibrium state. In contrast, the velocity in Figure 5.21 is clearly diverging after the rudder input for the 18% damage case. The divergence is

due to the controls forcing the aircraft outside the region of attraction of the level trim.

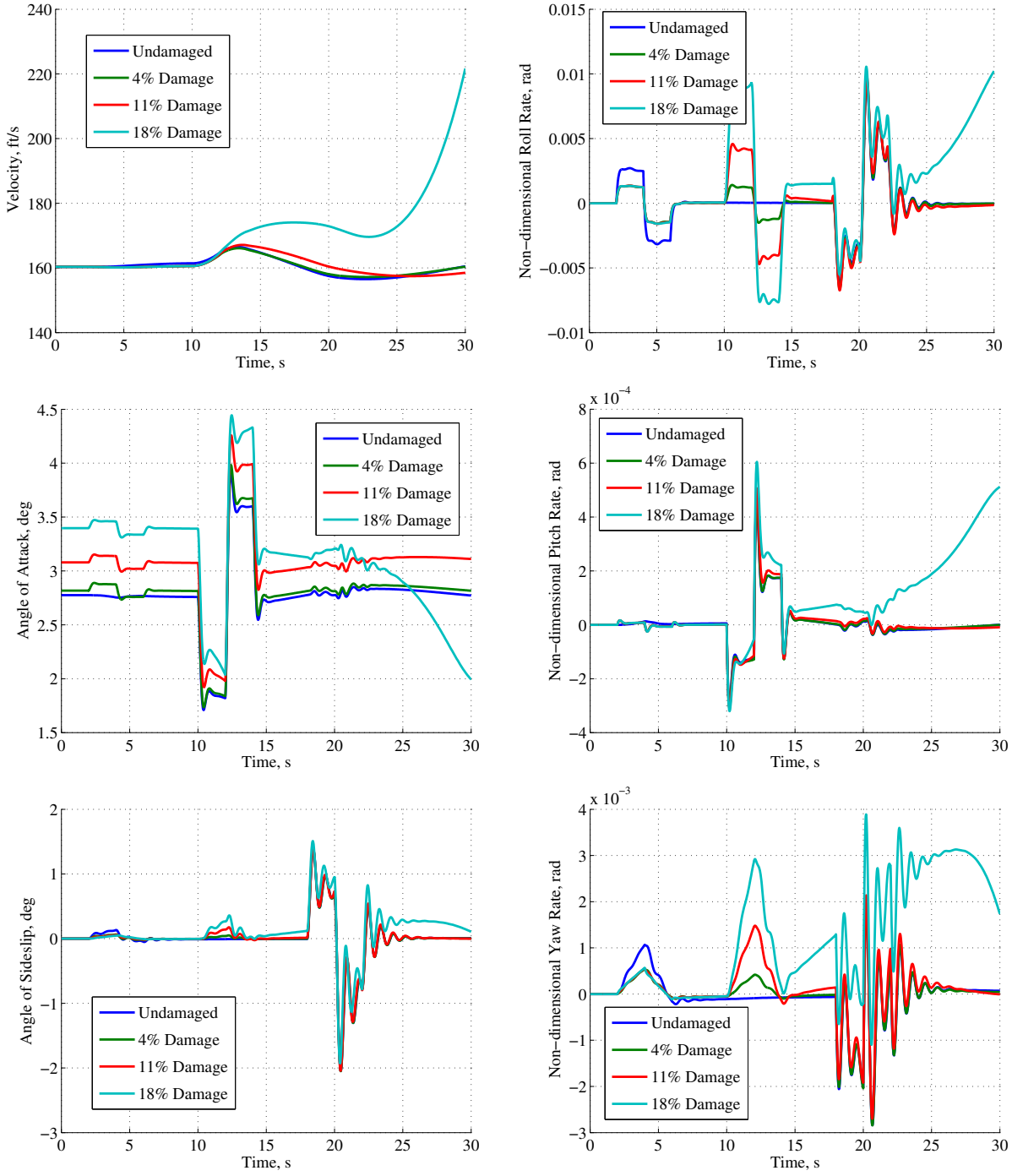

Figure 5.21: Time History of Doublet Input Response of an Initially Level Aircraft

Figure 5.22 shows the response of an aircraft which is trimmed initially at a sideslip angle of $-4°$. As shown previously, negative sideslip reduces the aileron required to achieve the level trim for the larger damage cases. These simulations also demonstrate an added benefit for the region of attraction. The elevator input still causes a large increase in the velocity. Yet, the states appear to be converging back to the equilibrium, which suggests that the control input does not force the system outside the region of attraction of the equilibrium.

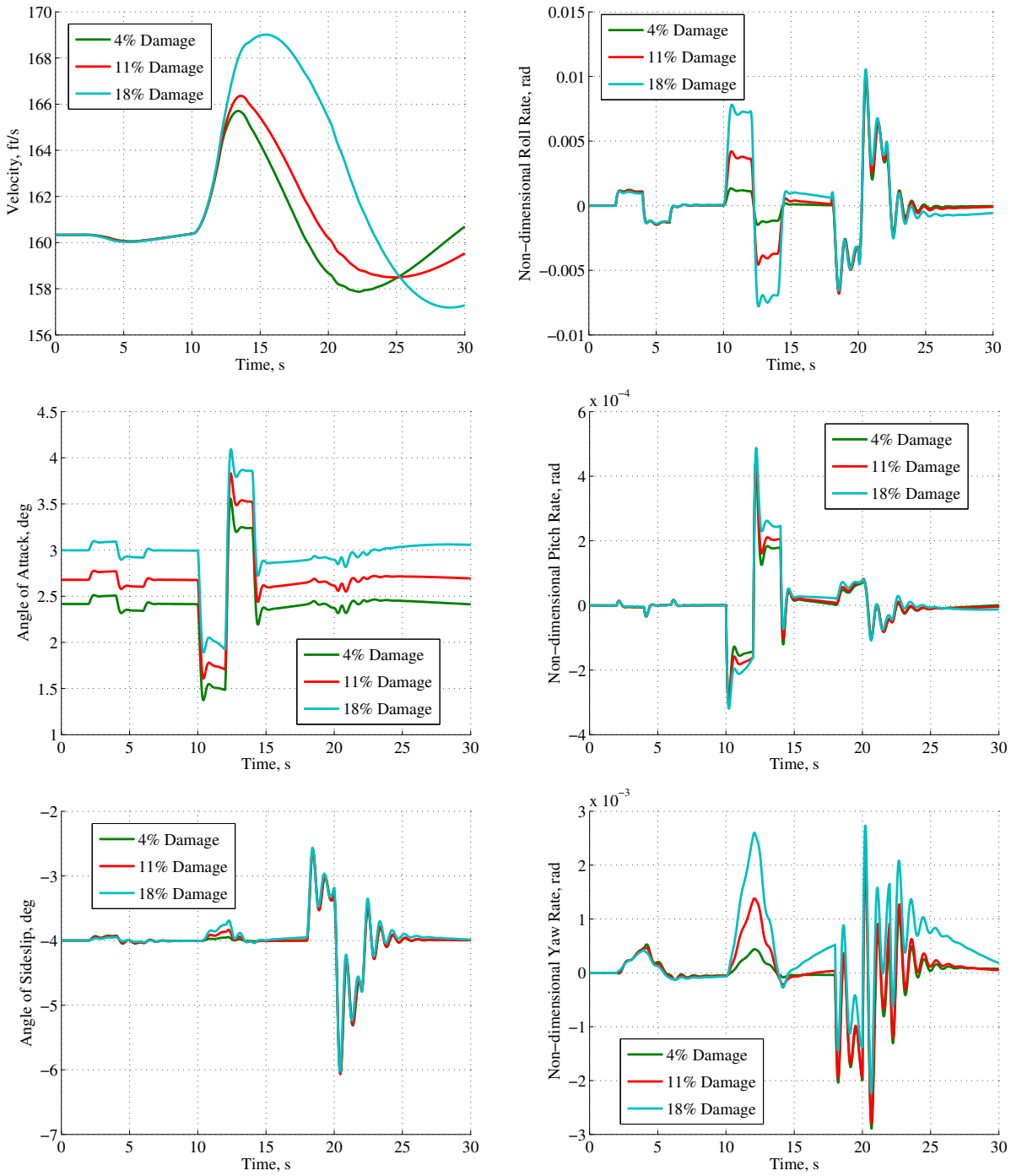

Figure 5.22: Time History of Doublet Input Response of an Initially Level Aircraft at Negative Sideslip ($\beta = -4$)

5.2.3 Coordinated Turn

In addition to the level trim case, one can consider an aircraft that is trimmed at a coordinated turn such that sideslip is zero and the radius of the turn is 1000 ft. Again the first consideration is the stability of the trim.

5.2.3.1 Stability of the Trim

The root locus for a coordinated turn is shown in Figure 5.23. Because the damage causes the aircraft to be asymmetric, the stability of the trim is different if the turn is to port or to starboard. For the turning to port, there is a very low frequency and lightly damped second order mode that is going unstable between 4% and 11% damage. Also, for the 33% tip loss, there is coalescence of the two first order modes into a highly damped second order mode.

For the turn to starboard, there is still an unstable mode, but it is not the same mode which goes unstable. It is the slow first order mode which goes unstable. Furthermore, it is unstable even for 4% damage.

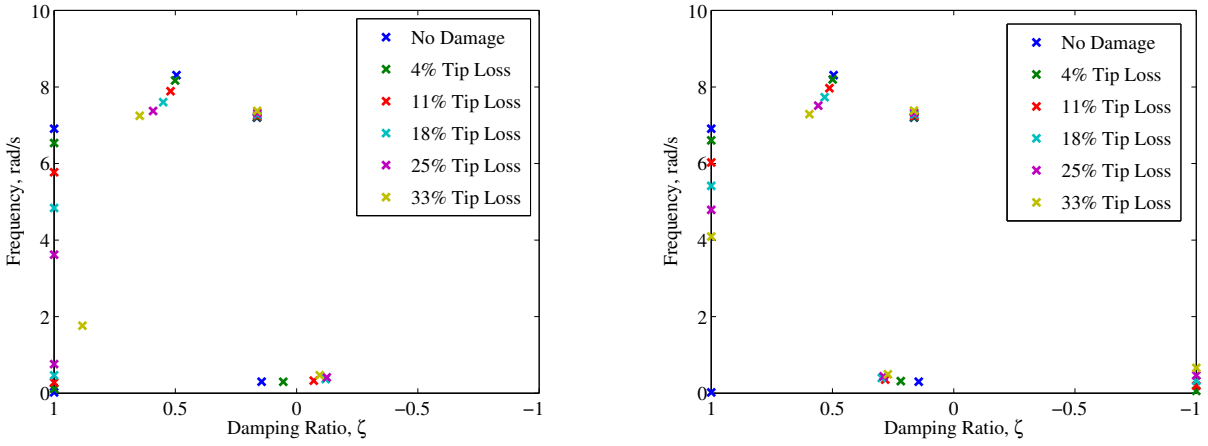

(a) Turning to Port

(b) Turning to Starboard

Figure 5.23: Root Locus of Damaged Aircraft in Coordinated Turn

5.2.3.2 Re-trimmed Simulation

For the coordinated turn, open loop simulations were performed to show the response to damage. The aircraft is initially undamaged for a coordinated turn with a radius of 1000 ft. After 10 seconds the damage occurs and the control surfaces switch to the new trim position, which was determined a priori.

The trajectory for the response of the aircraft with 18% damaged is shown in Figure 5.24. Since the coordinated turn is an unstable equilibrium for 18% damage, the ground path shows clear divergent behavior. Since the unstable mode has very small negative damping, the divergence is very slow.

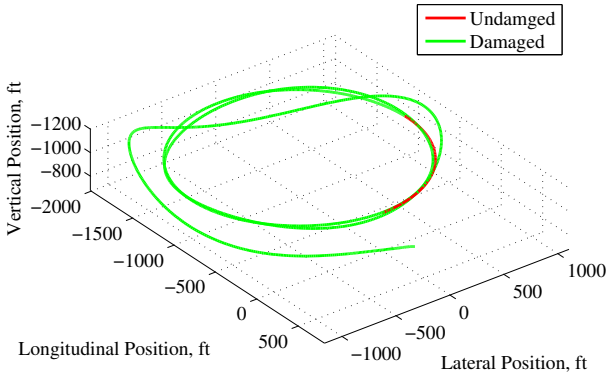

Figure 5.24: Trajectory of Response to 18% Damage of an Initially Turning Aircraft

The aircraft's time history for additional damage cases is shown in Figure 5.25. As the stability analysis showed, the 4% damage case is stable and converges to the trim state. In contrast, the 11% and 18% damage cases were shown to be unstable resulting in the divergent behavior seen in these simulations.

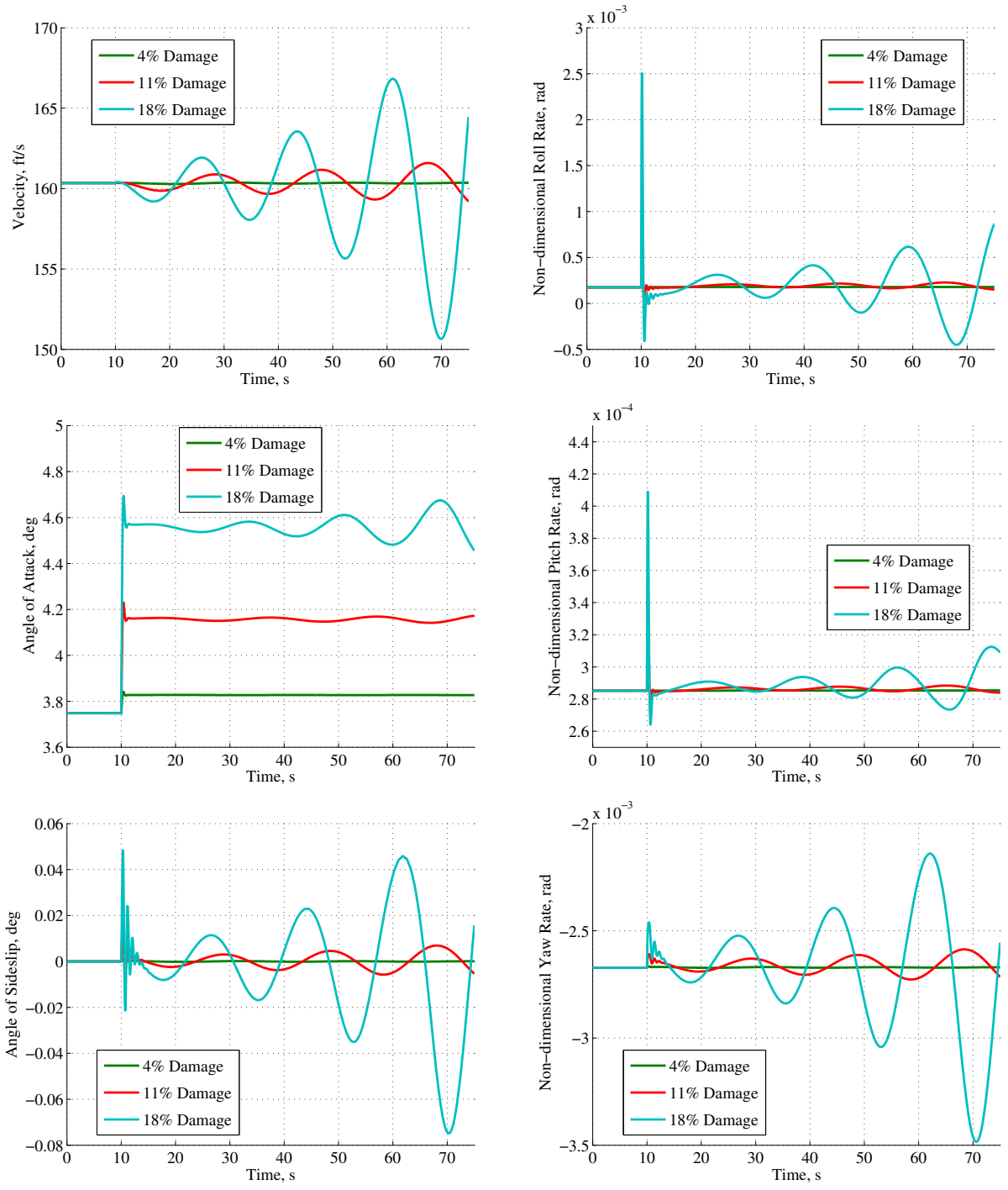

Figure 5.25: Time History Response to Damage of an Initially Turning Aircraft

5.3 Flight Loads

The results of the flight dynamics analysis was used to examine several cases of the loads on the aircraft structure. The distributed loads at trim were used to determine where the damage has the most significant effect. The time varying loads were then examined for the aircraft maneuvers simulated in Section 5.2.

5.3.1 Verification

For verification of the integration of the loads, the three test cases in Table 5.6 were used. These cases were selected to show the loads at trim and for two different cases with control deflection and non-zero angular rates.

Table 5.6: Aerodynamic Load Verification Cases

	Case 1	Case 2	Case 3
Velocity, ft/s	160.3	160.3	163.0
Angle of Attack, deg	2.745	2.738	1.821
Angle of Sideslip, deg	0	0.1154	-6.86×10^{-3}
Roll Rate, rad	0	2.93×10^{-3}	18.1×10^{-6}
Pitch Rate, rad	0	4.58×10^{-6}	-0.14×10^{-3}
Yaw Rate, rad	0	0.66×10^{-3}	-76.1×10^{-6}
Elevator Deflection, deg	3.0578	3.0578	4.0578
Aileron Deflection, deg	0.504×10^{-6}	1.00	0.504×10^{-6}
Rudder Deflection, deg	-1.41×10^{-6}	-1.41×10^{-6}	-1.41×10^{-6}
Altitude, ft	625	625	613.9

For each of these cases the loads were calculated in AVL and in the present simulation without correction factors and without rotation. Table 5.7 shows the resulting loads for each test case. The slight difference in the values of M_X and M_Y are likely errors due to the curve fit of the reduced-order model. The values of the drag are much smaller then the lift values. As a result of the limited precision of the AVL output, the M_Z do not match as well. However, these values are much smaller than the other loads and will not lead to a significant error in the total loads on the wing.

Table 5.7: Aerodynamic Load Verification

		Case 1	Case 2	Case 3
Current	M_X, ft-lb	−43.56	−43.27	−34.86
Simulation	M_Y, ft-lb	−21.91	−21.73	−18.22
	M_Z, ft-lb	0.97	0.93	1.42
AVL	M_X, ft-lb	−43.15	−42.91	−34.34
Output	M_Y, ft-lb	−21.81	−21.65	−18.04
	M_Z, ft-lb	0.48	0.48	1.13

5.3.2 Trim Loads

5.3.2.1 Level Trim

As a nominal case, the wing level trim without sideslip is shown in Figure 5.26. The distribution of loads is symmetric for the undamaged aircraft. 5.2.2 showed that the level trim solution of the damaged aircraft had a rudder deflection, which caused a bending moment applied to the wing root resulting in the discontinuity of the bending moment in Figure 5.26. The port wing exhibits a reduction in the bending moment due in part to the reduction in the wing span. The starboard wing bending is reduced by the large aileron deflection.

The damaged aircraft's asymmetric geometry results in an asymmetric torsion distribution. The pitching moment causes the discontinuity seen at the wing root. The torsion also has a discontinuity midspan due to a concentrated torsion applied by the engines. The aileron deflection required to trim the damaged aircraft causes a large change in the torsion on the starboard wing. The aileron deflection can reduce the torsion for smaller damage cases. For the larger damage cases, the aileron deflection results in an increase in the magnitude for sections of the wing.

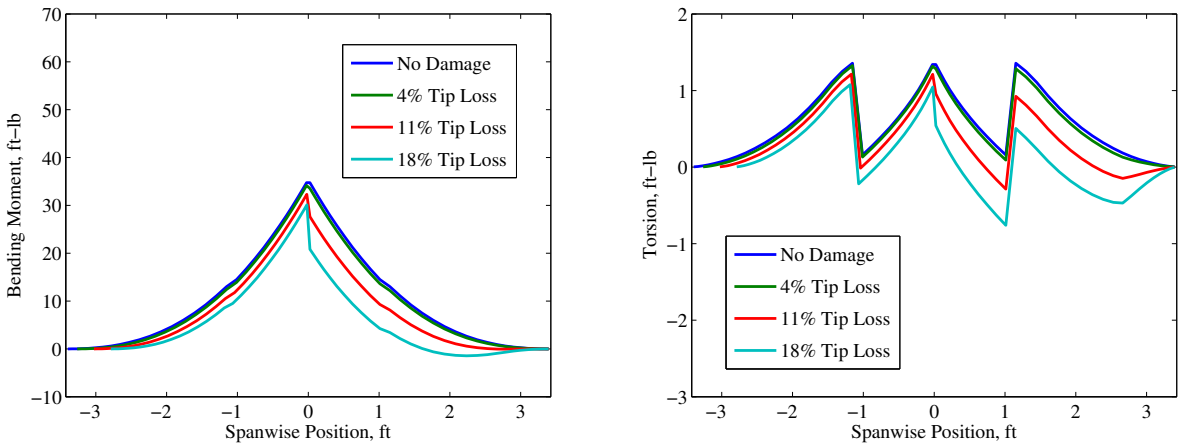

Figure 5.26: Wing Bending and Torsion at Level Trim

5.3.2.2 Steady Pull-up

To show a more severe case of wing loading, the distribution of forces for a steady 2-g pull-up maneuver are shown in Figure 5.27. As with the level trim, the undamaged aircraft exhibits a symmetric load distribution. For the pull-up maneuver the bending behaves very similarly to the level trim case. The pull-up maneuver demonstrates how the increased angle of attack for the damaged aircraft results in a decreased bending moment. The change in angle of attack changes the orientation of the lift forces with respect to the structural axis, resulting in a smaller bending moment. However, change in the orientation of the lift results in an increased fore-aft bending moment in Figure 5.27. As a result, the bending moment for the 2-g pull-up is not double the bending moment for the level trim.

A pull-up maneuver requires a large lift force, which generates a large rolling moment in the damaged aircraft. As a result, the effect of the aileron on the wing torsion is much more dramatic than for the level flight case.

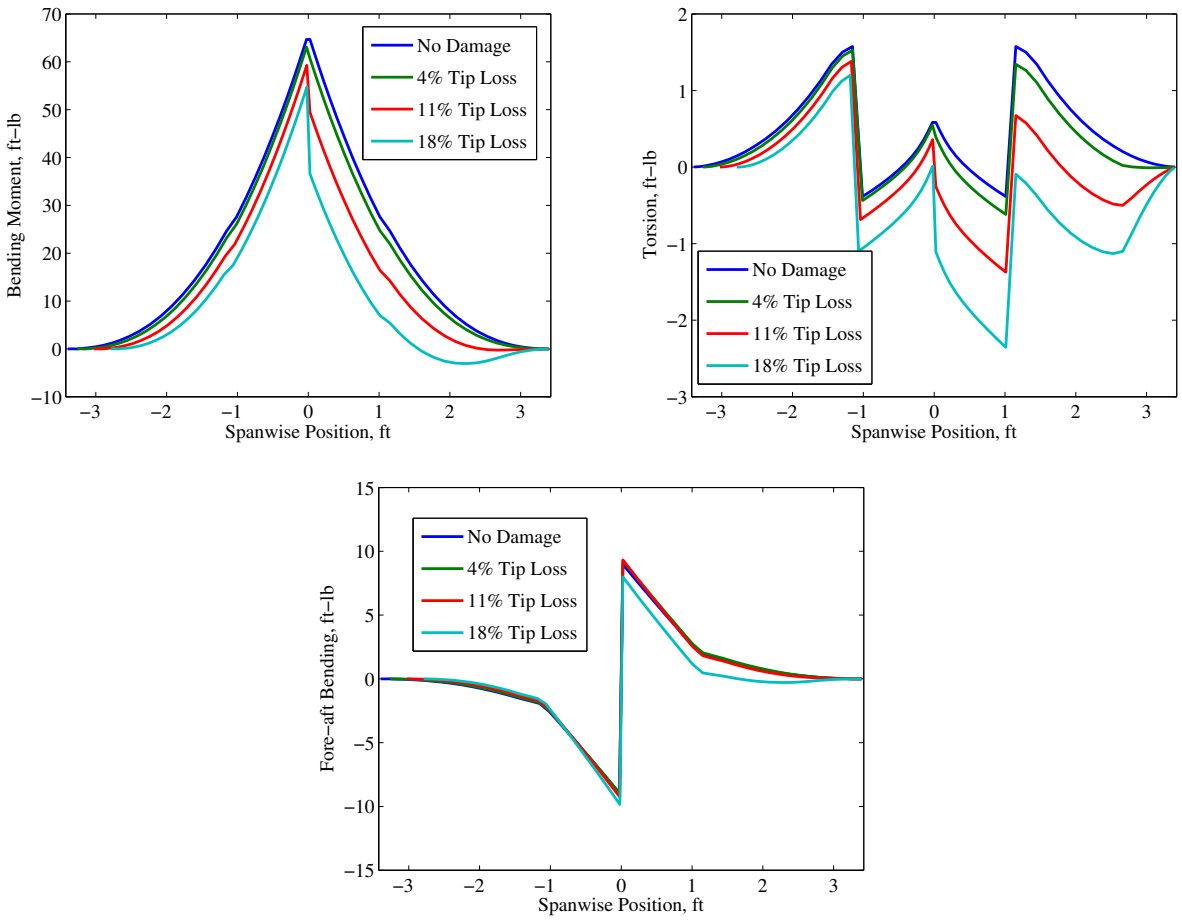

Figure 5.27: Wing Bending and Torsion in Steady Pull-up

5.3.3 Transient Loads

To further examine the effect of the damage on these loads, the loads were examined for the stick-fixed simulations and the doublet inputs with and without sideslip. The root bending and torsion loads for the starboard (undamaged) wing were examined since the trim loads suggest that the damage causes the most significant variation in the loads on the wing.

5.3.3.1 Stick-Fixed Simulation

After the damage there is initially a reduction in the bending moment in Figure 5.28. However, the previous stick-fixed simulations demonstrated a divergence of the aircraft's speed. Eventually, the large velocity becomes a dominant effect and results in the divergent loads.

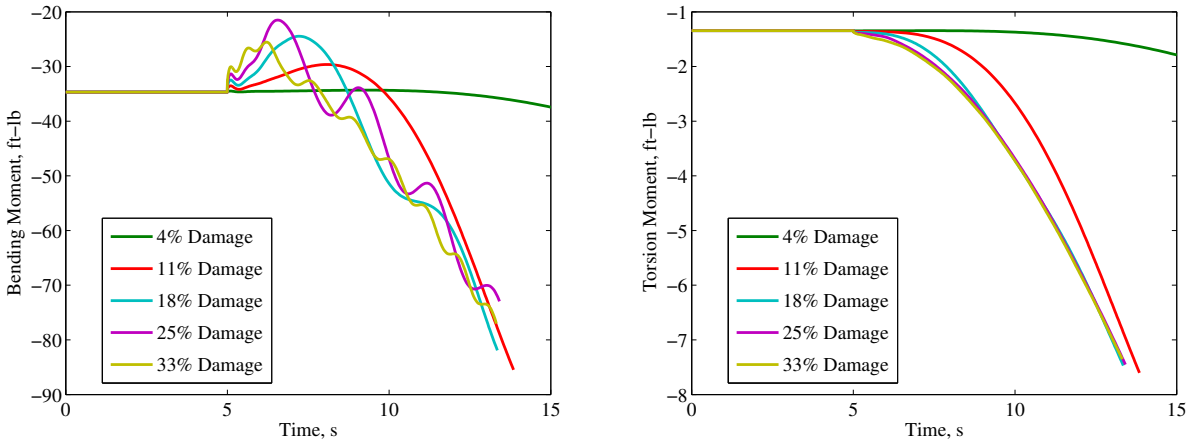

Figure 5.28: Maneuver Loads of Stick-Fixed Response to Damage of an Initially Level Aircraft

5.3.3.2 Doublet Inputs

To show the effect of the controls on the structural loads, the loads for the previous doublet input without sideslip are shown in Figure 5.29. The small aileron and rudder inputs do not have a significant impact on the wing bending. In contrast the elevator inputs cause a large change in the angle of attack. As a result, there is a large change in the wing bending moment. With the exception of the 18% damage case, the loads for each of these damage cases behave very similarly. The difference in the 18% damage case is due to the divergent flight dynamics seen earlier.

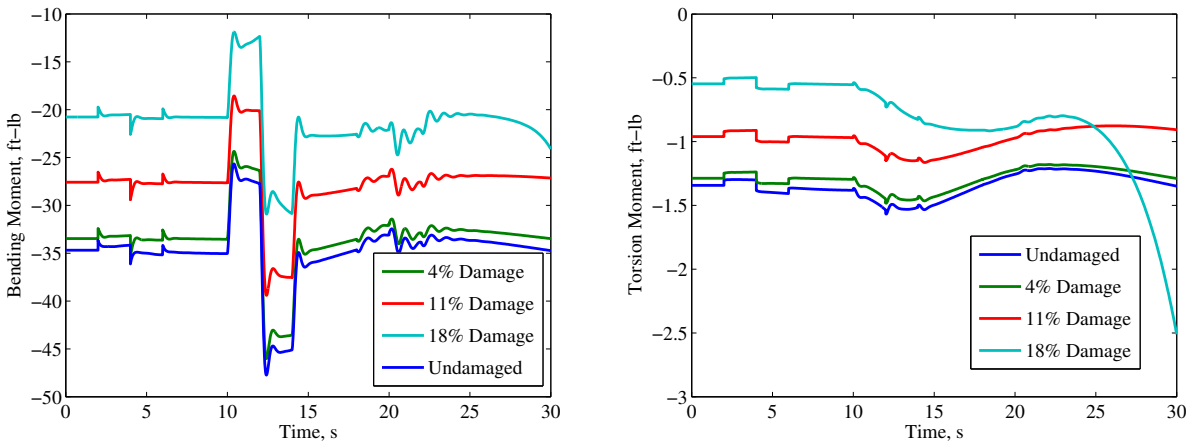

Figure 5.29: Maneuver Loads Due to Doublet Inputs of an Initially Level Aircraft

The loads for the doublet inputs of an aircraft trimmed at negative sideslip are shown in Figure 5.30. Negative sideslip results in an increase in these root loads. Yet, the general behavior of the loads remains quite similar. The primary difference is that the 18% damage case no longer diverges.

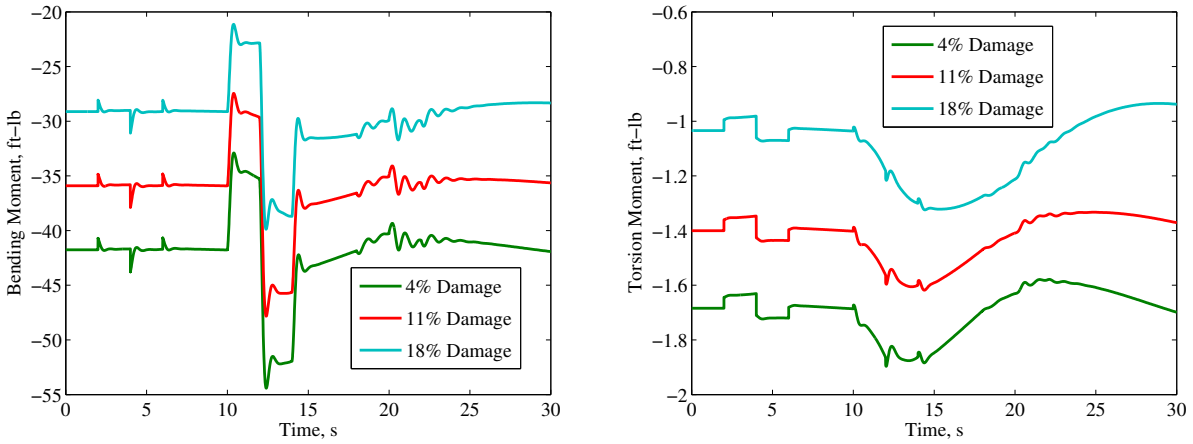

Figure 5.30: Maneuver Loads Due to Doublet Inputs of an Initially Level Aircraft at Negative Sideslip ($\beta = -4$)

Chapter 6

Conclusions and Future Work

6.1 Conclusions

This thesis studied the rigid body motion of a damage aircraft and the structural loads which result from that motion. Equations of motion were used which model the instantaneous change in inertial properties such as the center of gravity and the inertia matrix. The extended vortex lattice code AVL was used to generate snapshots of the aerodynamics loads over the linear flight envelope. These snapshots were then used to generate a reduced-order model with quadratic terms.

The structural loads considered the inertial, gravitational, aerodynamic, and propulsive forces. These forces were calculated in the body axis system and then rotated to a structural axis to separate the bending moments and torsion on the wing.

Examination of the flight dynamics of the generic transport model show that the damage led to a significant aileron deflection which complicates the determination of a trim. The level trim was shown to be stable for each of the cases where the ailerons did not reach saturation. In contrast, the coordinated turn showed instabilities for several damage cases. However, the nature of this instability was depended in the direction of the turn. Simulations were also used to show the aircraft's response to damage and the response of the damage aircraft to

control inputs.

The structural loads on the GTM were evaluated at several trim conditions to show the effect of the damage on the distribution of forces. In addition, simulations of the root bending were performed to show how the loads vary as the aircraft is maneuvering.

6.2 Future Work

These models of the flight dynamics and the structural loads will enable investigation of structural effects as well as the development of more sophisticated models of the aircraft's behavior. Some possible areas of further investigation include:

- The simulations suggested the damage may have a significant effect on the region of attraction of the trim conditions. The Lyapunov direct method could be used to examine these effects further.
- The damaged aircraft's loads can be used to examine the survivability of the aircraft's structure which may contain cracks or other degradation of its integrity.
- This loads model can be used to evaluate the adaptive control laws in development and to allow these laws to consider directly the structural loads.
- The aerodynamics load model can be coupled with a structural dynamics model to give an aeroservoelastic model of a damaged aircraft. This is important for high frequency inputs such as gust loading or due to control system adaptations.

Bibliography

[1] Rawlins, T. D., "High-Incidence Stabilator as an Out of Control Recovery Device for a Fixed-Wing Subscale Transport Unmanned Air Vehicle," *43rd AIAA Aerospace Sciences Meeting & Exhibit*, 2005.

[2] "Statistical Summary of Commercial Jet Airplane Accidents: Worldwide Operations 1959-2008," Tech. rep., Boeing: Commercial Airplanes, 2009.

[3] Russell, P. and Pardee, J., "JSAT Loss of Control: CAST Approved Final Report," Tech. rep., Commercial Aviation Safety Team, 2000.

[4] "NASA - Aviation Safety Program Fact Sheet," http://www.aeronautics.nasa.gov/pdf/avsafe_fs.pdf.

[5] "Integrated Resilient Aircraft Control Technical Plan," Tech. rep., National Aeronautics and Space Administration: Aeronautics Research Mission Directorate, 2007.

[6] Cunningham, K., Foster, J. V., Morelli, E. A., and Murch, A. M., "Practical Application of a Subscale Transport Aircraft for Flight Research in Control Upset and Failure Conditions," *AIAA Atmospheric Flight Mechanics Conference and Exhibit*, 2008.

[7] Jordan, T., Langford, W., Belcastro, C., Foster, J., Shah, G., Howland, G., and Kidd, R., "Development of a Dynamically Scaled Generic Transport Model Testbed for Flight Research Experiments," National Aeronautics and Space Administration.

[8] Jordan, T. L., Langford, W. M., and Hill, J. S., "Airborne Subscale Transport Aircraft Research Testbed - Aircraft Model Development," *AIAA Guidance, Navigation, and Control Conference and Exhibit*, 2005.

[9] Beltramo, M. N., Trapp, D. L., Kimoto, B. W., and Marsh, D. P., "Parametric Study of Transport Aircraft Systems Cost and Weight," Tech. rep., National Aeronautics and Space Administration, 1977.

[10] Woo, J.-H., "Static Aeroelastic Analysis of A Maneuvering Aircraft with Damaged Wing," *Aerospace Sciences Meeting and Exhibit*, 1992.

[11] Render, P. M., Samad-Suhaeb, M., Yang, Z., and Mani, M., "Aerodynamics of Battle-Damaged Finite-Aspect Ratio Wings," *Journal of Aircraft*, Vol. 46, 2009, pp. 997–1004.

[12] Foster, J. V., Cunningham, K., Fremaux, C. M., Shah, G. H., Stewart, E. C., Rivers, R. A., Wilborn, J. E., and Gato, W., "Dynamics Modeling and Simulation of Large Transport Airplanes in Upset Conditions," *AIAA Guidance, Navigation and Control Conference and Exhibit*, 2005.

[13] Shah, G. H., "Aerodynamic Effects and Modeling of Damage to Transport Aircraft," *AIAA Atmospheric Flight Mechanics Conference and Exhibit*, 2008.

[14] Thomas, A. L. R., "The aerodynamic costs of asymmetry in the wings and tail of birds: asymmetric birds can't fly round tight corners," *Proceedings: Biological Sciences*, Vol. 254, 1993, pp. 181–189.

[15] Keller, J. D., Robert M. McKillip, J., and Wachspress, D. A., "Physical Modeling of Aircraft Upsets for Real-Time Simulation Applications," *AIAA Atmospheric Flight Mechanics Conference and Exhibit*, 2008.

[16] Wilborn, J. E. and Foster, J. V., "Defining Commercial Transport Loss-of-Control: A Quantitative Approach," *AIAA Atmospheric Flight Mechanics Conference and Exhibit*, 2004.

[17] Bacon, B. J. and Gregory, I. M., "General Equations of Motion for a Damaged Asymmetric Aircraft," *AIAA Atmospheric Flight Mechanics Conference and Exhibition*, 2007.

[18] Nguyen, N., Krishnakumar, K., Kaneshige, J., and Nespeca, P., "Dynamics and Adaptive Control for Stability Recovery of Damaged Asymmetric Aircraft," *AIAA Guidance, Navigation, and Control Conference and Exhibit*, 2006.

[19] Nguyen, N., Krishnakumar, K., Kaneshige, J., and Nespeca, P., "Flight Dynamics and Hybrid Adaptive Control of Damaged Aircraft," *Journal of Guidance, Control, and Dynamics*, Vol. 31, No. 3, 2008, pp. 751–764.

[20] Nguyen, N., Krishnakumar, K., and Kaneshige, J., "Erratum on "Flight Dynamics and Hybrid Adaptive Control of Damaged Aircraft"," *Journal of Guidance, Control, and Dynamics*, Vol. 31, No. 6, 2008, pp. 1837–1838.

[21] Liu, Y., Tao, G., and Joshi, S. M., "Modeling and Model Reference Adaptive Control of Aircraft with Asymmetric Damage," *AIAA Guidance Navigation and Control Conference*, 2009.

[22] Sarigul-Klijn, N., Nespeca, P., Marchelli, T., and Sarigul-Klijn, M., "An Approach to Predict Flight Dynamics and Stability Derivatives of Distressed Aircraft," *AIAA Atmospheric Flight Mechanics Conference and Exhibit*, 2008.

[23] Pandita, R., Chakraborty, A., and Seiler, P., "Reachability and Region of Attraction Analysis Applied to GTM Dynamic Flight Envelope Assessment," *AIAA Guidance, Navigation, and Control Conference*, 2009.

[24] Kier, T. M. and Looye, G. H., "Unifying Manoeuvre and Gust Loads Analysis Models," *International Forum on Aeroelasticity and Structural Dynamics*, 2009.

[25] Patil, M. J., "Nonlinear Gust Response of Highly Flexible Aircraft," *AIAA/ASME/ASCE/AHS/ASC Structures, Structural Dynamics, and Materials Conference*, 2007.

[26] Raveh, D. E., "Maneuver Load Analysis of Overdetermined Trim Systems," *Journal of Aircraft*, Vol. 45, 2008, pp. 119 – 129.

[27] Conyers, H. J., Dowell, E. H., and Hall, K. C., "Aeroelastic Studies of a Rectangular Wing with a Hole: Correlation of Theory and Experiment," *NBSE Aerospace Systems Conference*, 2010.

[28] Smith, T. A., Nielsen, Z. A., Reichenbach, E. Y., and Sr., J. M. U., "Dynamic Structural Fault Detection and Identification," *AIAA Guidance Navigation and Control Conference*, 2009.

[29] Nelson, R. C., *Flight Stability and Automatic Control*, McGraw-Hill, Inc., 1998.

[30] Stevens, B. L. and Lewis, F. L., *Aircraft Control and Simulation*, John Wiley and Sons, Inc., 2003.

[31] Khalil, H. K., *Nonlinear Systems*, Prentice Hall, 2002.

[32] Palm, W. J., *System Dynamics*, McGraw-Hill, Inc., 2005.

[33] Hibbeler, R. C., *Engineering Mechanics: Statics and Dynamics*, Prentice Hall, 2004.

[34] Drela, M. and Youngren, H., *AVL 3.26 User Primer*, http://web.mit.edu/drela/Public/web/avl/avl_doc.txt, April 2006.

[35] Logan, D. L., *A First Course in the Finite Element Method*, Thompson, 2007.

[36] Cox, D., "GTM Design-Simulation Model v0912," 2010.

[37] "CAD 3-View Drawings for Airport Planning Purposes," http://www.boeing.com/commercial/airports/dwgs/7572.zip, 2008.

[38] Teper, G. L., "Aircraft Stability and Control Data," NASA Contractor Report CR-96008, National Aeronautics and Space Administration, 1969.

[39] Katz, J. and Plotkin, A., *Low-Speed Aerodynamics: From Wing Theory to Panel Methods*, McGraw-Hill, Inc., 1991.

Appendix A

Aerodynamic Model

The reference parameters are shown in Table A.1. In AVL the lifting surface is defined by the location of the leading edge, the chord, and the angle of twist. The control surface is defined by the location of the start of the hinge as a fraction of the chord, x_{hinge}/c_{ref}. The parameters for the lifting surfaces of the current model are shown in Table A.2. The fuselage is defined by the x-location and the upper and lower points of the circular cross section, shown in Table A.3.

Table A.1: Aerodynamic Model: Reference Parameters

Center of Gravity, ft	x_{ref}	3.8468
	y_{ref}	0.0000
	z_{ref}	-0.1804
Area S_{ref}, ft^2		4.9850
Wing Span b_{ref}, ft		0.8317
Wing Chord c_{ref}, ft		6.2418

Table A.2: Aerodynamic Model: Lifting Surfaces

		Leading Edge, ft			Chord, ft	Twist, deg	Control Hinge
		x_{le}	y_{le}	z_{le}			x_{hinge}/c_{ref}
Wing	Root	2.8002	0.0000	-0.1969	1.5043	0.00	
		3.4760	1.2451	-0.0886	0.8301	0.00	
		4.0781	2.3622	0.0098	0.5036	-1.20	0.79
		4.4537	3.0561	0.0705	0.3018	-1.94	0.78
	Tip	4.4833	3.1119	0.0755	0.2838	-2.00	
Horizontal Tail	Root	6.6273	0.0000	0.0410	0.8186	-3.20	
		6.7454	0.1706	0.0623	0.7448	-3.20	0.71
	Tip	7.4885	1.2467	0.1985	0.2789	-3.20	0.67
Vertical Tail	Root	5.8875	0.0000	0.0000	1.2976	0.00	
		6.1106	0.0000	0.2247	1.1614	0.00	0.64
	Tip	7.3622	0.0000	1.4911	0.4003	0.00	0.68

Table A.3: Aerodynamic Model: Fuselage

X Position	Top	Bottom
0.0000	-0.1389	-0.1389
0.2500	-0.2302	0.0723
0.5000	-0.2823	0.2263
0.7500	-0.3004	0.3236
1.0000	-0.2953	0.3625
1.5000	-0.2953	0.3625
2.0000	-0.2953	0.3625
3.0000	-0.2953	0.3625
4.0000	-0.2953	0.3625
5.0000	-0.2953	0.3625
5.5000	-0.2875	0.3624
6.0000	-0.2565	0.3528
6.2500	-0.2294	0.3414
6.5000	-0.1933	0.3241
6.7500	-0.1474	0.3001
7.0000	-0.0908	0.2685
7.2500	-0.0228	0.2285
7.5000	0.0574	0.1794
7.7034	0.1322	0.1322

Appendix B

AVL Vortex Lattice Extensions

The present work used the extended vortex lattice code AVL to model the 3-D aerodynamics of the aircraft. There are several extensions to this vortex lattice method (VLM) to capture the effects of the airfoil lift curve slope, the chamber, compressible subsonic flow, slender bodies, and viscous forces[34].

The airfoil lift curve slope, chamber, and compressibility effects are captured by changes to the vortex lattice calculations. Typically a vortex lattice method enforces a no penetration boundary condition at the ¾ point on the vortex panel. By altering the point where the no penetration boundary condition is enforced, AVL will model a different lift curve slope. The direction of this no penetration boundary condition can also be changed. This will model the chamber in the wing assuming small angles. The compressibility effects are modeled by a Prandtl-Glauert correction, which will adjust for the subsonic flow.

The results of the VLM are used to determine the forces slender bodies in the flow and due to viscous forces. AVL uses a discretization of slender body theory[39] to model these bodies in the wing's flow field. A series of discrete doublets and sources are distributed along the centerline of the body. The strength of these doublets and sources are determined by a no penetration boundary condition in the flow field from the VLM.

B.1 Viscous Forces

The viscous forces are broken into two types, those due to the lifting surfaces and those due to slender bodies. The drag from the slender bodies is assumed to be constant and is known a priori. As the damage considered here is only on the lifting surfaces, AVL is able to account for the effect of the damage on the drag. This results in a constant which is added to the final integrated forces.

Determination of the viscous forces on the lifting surfaces requires three points on the drag polar for the airfoil, shown in Figure B.1. The drag force is then modeled by 4 quadratic functions. These functions are determined such they are smooth and continuous at each of the three input points. Furthermore, the slope at (C_{D_0}, C_{L_0}) is forced to be zero. Although AVL does estimate the drag polar beyond the stall point, this is not used in the present work since this will violate the linear assumptions used for the vortex lattice method.

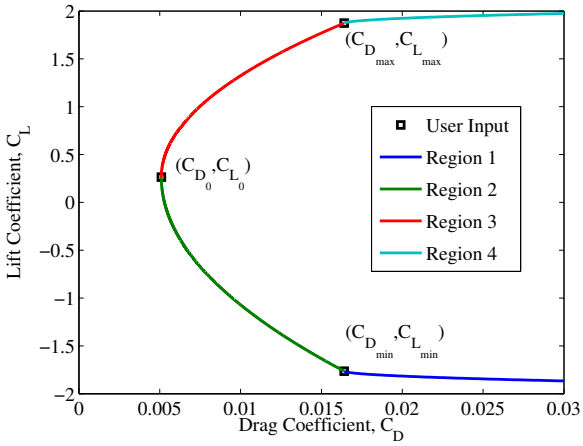

Figure B.1: AVL Approximation of the Airfoil Drag Polar

AVL uses the lift distribution from the vortex lattice method along with this drag polar to determine the distribution of the drag forces. The drag forces are then added to the VLM results and integrated.